



Validation of Global EUV Wave MHD Simulations and Observational Techniques

Cooper Downs¹ , Alexander Warmuth² , David M. Long³ , D. Shaun Bloomfield⁴ , Ryun-Young Kwon⁵ ,Astrid M. Veronig^{6,7} , Angelos Vourlidas⁸ , and Bojan Vršnak⁹ ¹ Predictive Science Inc., 9990 Mesa Rim Road, Suite 170, San Diego, CA 92121, USA; cdowns@predsci.com² Leibniz-Institut für Astrophysik Potsdam (AIP), An der Sternwarte 16, 14482 Potsdam, Germany³ UCL-Mullard Space Science Laboratory, Holmbury St. Mary, Dorking, Surrey, RH5 6NT, UK⁴ Northumbria University, Newcastle upon Tyne, NE1 8ST, UK⁵ Korea Astronomy and Space Science Institute, Daejeon 34055, Republic of Korea⁶ Institute of Physics, University of Graz, A-8010 Graz, Austria⁷ Kanzelhöhe Observatory for Solar and Environmental Research, University of Graz, A-8010 Graz, Austria⁸ The Johns Hopkins University Applied Physics Laboratory, Laurel, MD 20723, USA⁹ Hvar Observatory, Faculty of Geodesy, Kaciceva 26, 10000 Zagreb, Croatia

Received 2020 August 19; revised 2021 February 22; accepted 2021 February 25; published 2021 April 23

Abstract

Global EUV waves remain a controversial phenomenon more than 20 yr after their discovery by SOHO/EIT. Although consensus is growing in the community that they are most likely large-amplitude waves or shocks, the wide variety of observations and techniques used to identify and analyze them have led to disagreements regarding their physical properties and interpretation. Here, we use a 3D magnetohydrodynamic (MHD) model of the solar corona to simulate an EUV wave event on 2009 February 13 to enable a detailed validation of the various commonly used detection and analysis techniques of global EUV waves. The simulated event exhibits comparable behavior to that of a real EUV wave event, with similar kinematic behavior and plasma parameter evolution. The kinematics of the wave are estimated via visual identification and profile analysis, with both approaches providing comparable results. We find that projection effects can affect the derived kinematics of the wave, due to the variation in fast-mode wave speed with height in the corona. Coronal seismology techniques typically used for estimates of the coronal magnetic field are also tested and found to estimate fast-mode speeds comparable to those of the model. Plasma density and temperature variations of the wave front are also derived using a regularized inversion approach and found to be consistent with observed wave events. These results indicate that global waves are best interpreted as large-amplitude waves and that they can be used to probe the coronal medium using well-defined analysis techniques.

Unified Astronomy Thesaurus concepts: [Solar corona \(1483\)](#); [Solar coronal mass ejections \(310\)](#); [Solar coronal waves \(1995\)](#); [Solar magnetic fields \(1503\)](#); [Solar extreme ultraviolet emission \(1493\)](#); [Magnetohydrodynamical simulations \(1966\)](#)

Supporting material: animations

1. Introduction

Ever since their discovery by Dere et al. (1997), Moses et al. (1997), and Thompson et al. (1998) using the Extreme ultraviolet Imaging Telescope (EIT; Delaboudinière et al. 1995) on board the Solar and Heliosphere Observatory (SOHO; Domingo et al. 1995), global waves in the low solar corona have been systematically observed using Extreme UltraViolet (EUV) passbands. Commonly called “EIT waves”, these phenomena have since been observed in the EUV using the Extreme UltraViolet Imager (EUVI; Wuelser et al. 2004) on board the Solar Terrestrial Relations Observatory (STEREO; Kaiser et al. 2008) and more recently by the Atmospheric Imaging Assembly (AIA; Lemen et al. 2012) on board the Solar Dynamics Observatory (SDO; Pesnell et al. 2012), the Sun Watcher with Active Pixels and Image Processing (SWAP; Seaton et al. 2013) on board the Project for On-Board Autonomy 2 satellite (*PROBA2*; Santandrea et al. 2013), and the Solar Ultraviolet Imager (SUVI; Seaton & Darnel 2018) on board the GOES-16 spacecraft. Despite a plethora of

observations and more than 20 yr of analysis, these features continue to be a source of investigation, with constant questions regarding their physical interpretation (Vršnak & Cliver 2008).

Global EUV waves were originally interpreted, using fast-mode linear wave theory, as the coronal counterpart of the chromospheric Moreton–Ramsey wave observed by Moreton (1960) and Moreton & Ramsey (1960). Apparent discrepancies between the observed and theoretical behavior of the phenomena have led to the development of a series of alternative interpretations for global EUV waves. Instead of being explained as fast-mode waves (Wang 2000), these features were instead interpreted as a signature of the coronal magnetic field restructuring during a solar eruption. In particular, “EIT waves” were variously interpreted as being due to either continuous small-scale magnetic reconnection (e.g., Attrill et al. 2007), Joule heating at the edge of a current shell formed between the erupting filament and the surrounding coronal magnetic field (e.g., Delannée et al. 2008), or stretching of magnetic field lines during a solar eruption (e.g., Chen et al. 2002). Alternative wave-based theories included interpreting “EIT waves” as slow-mode magnetohydrodynamic (MHD) waves (e.g., Wang et al. 2009), MHD solitons (e.g., Wills-Davey et al. 2007), or using a combination of both wave and nonwave theories



Original content from this work may be used under the terms of the [Creative Commons Attribution 4.0 licence](#). Any further distribution of this work must maintain attribution to the author(s) and the title of the work, journal citation and DOI.

(e.g., Zhukov & Auchère 2004). A comprehensive overview of the different potential theories proposed to explain the “EIT wave” phenomenon can be found in the review by Long et al. (2017b) and references therein.

While each proposed theory has its individual merits, no single theory has been able to account for all observed signatures of these events (Patsourakos & Vourlidas 2012). Much of the uncertainty surrounding the physical interpretation of these phenomena initially arose due to the very low spatial and temporal resolution of the instruments used to identify and characterize them. Although with the advent of SDO/AIA this issue has been greatly diminished, a myriad of techniques and approaches are still used to identify and characterize these features across a wide range of passbands observing plasma at different temperatures.

As they propagate through the low solar corona, global EUV waves potentially provide an opportunity to probe properties of the low solar atmosphere that remain frustratingly out of reach of current instrumentation. In particular, interpretation of these features as MHD waves offers the opportunity to estimate the coronal magnetic field using coronal seismology techniques (see, e.g., Ballai 2007; West et al. 2011; Kwon et al. 2013; Long et al. 2013, for previous work done on this topic). They are also closely associated with coronal mass ejections (CMEs) and can potentially provide insight into the direction and extent of the initial eruption (e.g., Temmer et al. 2011; Möstl et al. 2015; Long et al. 2019). However, their derived properties, such as their kinematics, can be potentially biased by the techniques used to identify and track these features (cf., Byrne et al. 2013), underlining the necessity for validation of these different techniques using a controlled data set with known properties.

Here we use a simulation of the 2009 February 13 global EUV wave observed by STEREO to validate a variety of the most commonly used techniques for identifying and analyzing EUV waves. With the simulation, all physical parameters are known during the evolution of the global wave, and they can be connected to their observable signatures. The particular event was chosen because it was observed in quadrature by the two STEREO spacecraft and was therefore very well studied (Section 2.1). This work is also intended to complement our prior work linking wave mechanisms to their observable properties (Long et al. 2017b), providing important physical context from a simulation that may help guide the general interpretation and analysis of global EUV waves. The event is summarized and the simulation outlined in Section 2. Section 3 applies and compares different techniques typically used to estimate the kinematics of global EUV waves. Section 4 examines the evolution of plasma density and temperature with the passage of the global EUV wave. Finally, Section 5 summarizes and discusses the results, before drawing some conclusions on the implications of this work.

2. The 2009 February 13 CME and Simulation

2.1. Context

The 2009 February 13 CME originated from NOAA AR 11012, with the rapid rise and low coronal onset occurring around 5:30 UT. At this time, the twin STEREO spacecraft were at quadrature ($\sim 90^\circ$ separation) and the eruption was observed almost at disk center by STEREO-B and just off the limb by STEREO-A. The preceding minimum offered an ideal

opportunity to study eruptions occurring in relatively simple, isolated configurations, and the 2009 February 13 CME event is a perfect example. Apart from AR 11012, there were no other active regions visible at the time, suggesting a largely dipolar corona consisting of mostly quiet Sun. This event has been studied by a number of authors (e.g., Kienreich et al. 2009; Patsourakos & Vourlidas 2009; Cohen et al. 2009; West et al. 2011; Warmuth & Mann 2011; Muhr et al. 2011; Miklenic et al. 2011; Attrill et al. 2014; Podladchikova et al. 2019) because it featured an ideal circular EUV wave propagating far from the eruption site and a symmetric pair of core dimming regions near the magnetic polarity inversion line.

The characteristics of this wave from both perspectives were cited as strong evidence for the fast-mode nature of the wave front by Patsourakos & Vourlidas (2009) and Kienreich et al. (2009). Both groups argued that the rapid expansion of the CME, forming an expanding bubble, acted as a driver of a fast-mode MHD wave that decoupled in the transverse directions. This result is consistent with the kinematic analysis of the STEREO-B wave front in the NW direction by other authors (Muhr et al. 2011; Warmuth & Mann 2011). This event was also studied from a wave seismological perspective by West et al. (2011), who employed spectroscopic observations of the nearby quiet Sun to estimate the local density of the medium as the wave passed. They derived a relatively low magnetic field strength (corresponding to a relatively large plasma β), and this result will be examined here.

Lastly, this event is relevant from an EUV wave modeling perspective. In their numerical modeling of the wave (one of the first studies of its kind), Cohen et al. (2009) argued for a hybrid EUV wave mechanism. Although a large-scale fast-mode wave produced a dome-like perturbation, they also found evidence in the simulation for some reconfiguration of the corona near the wave front and corroborated this behavior with the reconnection front cartoon of Attrill et al. (2007). By modeling the full 3D thermodynamic MHD evolution of this event, we significantly improve upon the Cohen et al. (2009) simulation in two aspects. First, they used a strongly out-of-equilibrium flux rope to model the CME, meaning that the balance of flux between the flux rope, the active region (AR), and the surrounding quiet-Sun field was skewed unrealistically, which can greatly alter when, where, and how much reconnection will occur. Second, the MHD model employed by Cohen et al. (2009) used the polytropic MHD approximation with a variable adiabatic index and an ad hoc coronal density and temperature distribution, making the ensuing thermodynamic evolution unreliable. This prohibited them from making a direct comparison of forward-modeled observables to observations, which is a key step in establishing the relevance of the simulation to the observed event.

For our simulation of the 2009 February 13 CME event, we used the Magnetohydrodynamic Algorithm outside a Sphere model (MAS; Lionello et al. 2009). MAS employs a “thermodynamic” MHD approach to model the global solar corona, where additional terms that describe energy flow in the corona and solar wind are included (coronal heating, parallel thermal conduction, radiative loss, and Alfvén wave acceleration). Solving for these terms allows the model to capture realistic coronal density and temperature stratifications, and enables the forward-modeling of synthetic EUV images and other observable diagnostics.

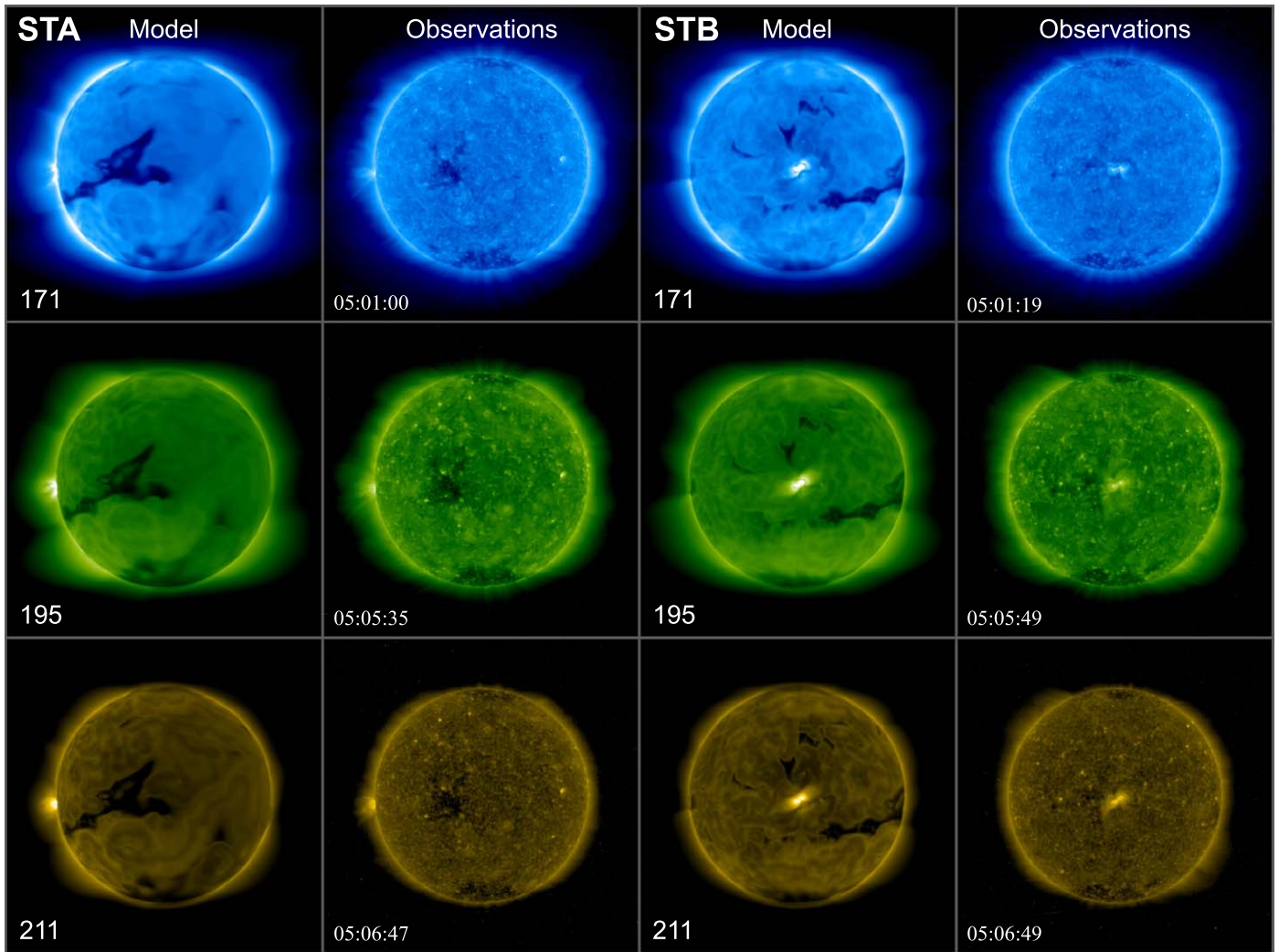


Figure 1. Pre-event comparison of observations to forward-modeled emission from the MHD model. Top to bottom rows: EUVI 171, 195, 284 Å channels. Right to left: STEREO-A (STA) simulation, STA observations, STEREO-B (STB) simulation, STB observations. The images are log-scaled the same way for each filter, including the same minimum and maximum.

When simulating EUV waves in a thermodynamic MHD model, there are two main elements to the modeling process: first, developing a suitable background coronal model for the event; and second, constructing a realistic eruptive configuration that can be destabilized slowly. We accomplish this in MAS using a similar setup and methodology to Török et al. (2018). These techniques improve significantly upon Cohen et al. (2009) as well as prior thermodynamic MHD simulations of EUV waves (Downs et al. 2011, 2012). The elements of the energization and destabilization process are largely summarized here; however, these details will appear in a forthcoming study on coronal dimming that is based on this simulation (Downs et al. 2021).

2.2. Modeling the Background Corona

The first step in the simulation is the development of a realistic 3D MHD background coronal solution using maps of the measured surface magnetic field as a boundary condition. For this particular case, we build a composite boundary condition starting with the LMSAL Evolving Surface-Flux Assimilation Model (Schrijver & De Rosa 2003) for an estimate of the radial component of the surface magnetic field

over the full Sun. On this map, we overlay higher-quality Global Oscillation Network Group (GONG) observations of the AR just prior to the eruption, converting from the measured line-of-sight component of the field to the required radial component using the standard geometric assumption that the measured field is radial. The 3D model is initialized with a potential field extrapolation using this boundary condition and then relaxed for a sufficiently long time that a stable thermal-magnetic configuration is reached in the corona.

Following a similar approach to Downs et al. (2013), the empirical heating model is parameterized to provide a decent multifilter match for average quiet-Sun intensities. To forward-model EUV emissivities, we use the CHIANTI 7.1 spectral synthesis package (Landi et al. 2013) and the STEREO/EUVI-A&B and SDO/AIA calibration information provided in SolarSoftWare IDL (SSW; Freeland & Handy 1998).

Figure 1 compares the forward-modeled EUVI images to STEREO-A and -B observations. As in the observations, the bright emission from AR 11012 is well contrasted from the surrounding quiet Sun off the east limb (STEREO-A) and at disk center (STEREO-B). A clear multifilter dependence of the global EUV emission and morphology is also present in both the observations and model. The largest discrepancies are

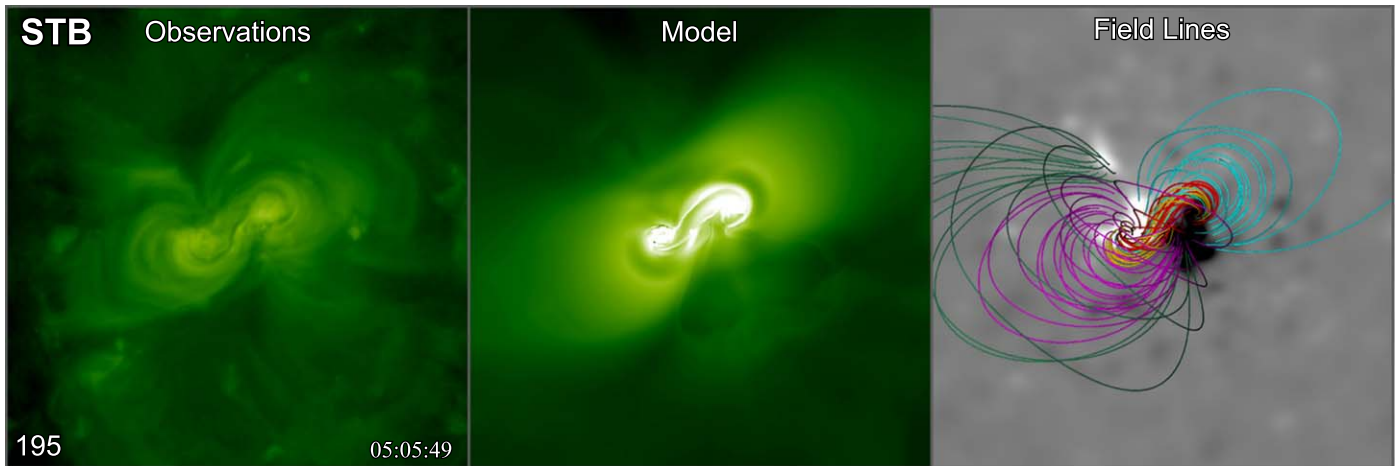


Figure 2. Zoomed-in comparison of the pre-event STEREO-B/EUVI 195 Å observations (left) to the MHD model, including forward-modeled EUVI 195 Å emission (middle) and the underlying field configuration (right). Both the core sigmoidal field structure and large shear of the surrounding arcade are well represented in the model. The 195 Å images are log-scaled with the same minimum and maximum.

regarding the positions of the equatorial coronal holes, including the large coronal hole (CH) to the southwest of the erupting AR that is nonexistent in the observations (STEREO-B view). The position and width of equatorial holes are strongly tied to the polar fields and flux balance of the surface magnetic field maps, which can be hard to capture accurately due to observational limitations.

The solution itself is run on a nonuniformly spaced $321 \times 427 \times 527$ spherical grid with the highest resolution in the AR core. Good resolution is maintained out to $\pm 90^\circ$ from the AR (i.e., the solar disk as seen by STEREO-B), with emphasis on the $\pm 45^\circ$ region. This is the reason for simulated structures appear finer nearer to the AR.

2.3. Eruption Model

The next step is to develop an energized, eruptive configuration in the AR of interest. Figure 2 shows the final energized state before the eruption. We do this by superposing a pair of modified Titov & Démoulin (TDm) flux ropes (Titov et al. 2014) onto the 3D background magnetic field in the model. The resulting field is then relaxed by advancing the MHD model, resulting in a sheared AR configuration containing large-scale currents with a stable, sigmoid-shaped flux rope at the core. As with Török et al. (2018), using TDm flux ropes in this manner is largely a trial-and-error process, done using observations and the strapping field of the overlying AR as a guide.

The most important step is driving the energized magnetic configuration to erupt. Here we design boundary electric fields that will cancel the radial field of the inserted flux rope at the inner boundary. This process simultaneously erodes the restraining strapping field and adds poloidal flux to the flux rope. In this case, there is a slow rise phase (whose timescale depends on driving) followed by a rapid acceleration (ideal evolution then reconnection). Driving lasts for about 40 minutes of physical time and is deliberately ramped down around the time of rapid onset.

For the remainder of the paper, we describe the portion of the simulation that includes the driving phase, eruption, and simulated EUV wave. This includes 270 snapshots of 3D model data, saved at a 24 s cadence. We link the start of rapid acceleration in the simulation (snapshot 98) to a physical time

of 5:35:35 UT. This allows us to assign a time stamp to each point of the simulation, which covers about 4:56–6:44 UT.

2.4. The Simulated EUV Wave

As the rapid rise and acceleration occur in the simulation, a CME forms and the bulk motion becomes super-Alfvénic above the AR. A rough estimate gives a bulk speed of about $300\text{--}350 \text{ km s}^{-1}$, which is similar to what was observed. At this time, a dome-shaped perturbation is clearly visible, and as it expands, the flanks propagate through the low corona.

A comparison of the simulated wave to observations is shown in Figure 3, along with some arrows marking the key features and a corresponding animation. Both the simulation and the observations show the classic picture of an EUV wave, namely a circular bright front that forms and becomes more diffuse as the front propagates over the solar disk. The NW evolution of the wave seems qualitatively similar in speed and appearance, which is quite encouraging. On the other hand, the circular intensity enhancement was less symmetric in the real event compared to the simulated one (compare the eastward versus westward evolution in the STEREO-B view). This is likely related to the coronal hole on the eastern boundary of the AR (seen in the STB observations in Figure 1), which can alter and inhibit the propagation of the disturbance into the quiet Sun and beyond (Patsourakos & Vourlidas 2009). As discussed in Section 2.2, this small coronal hole is not captured by the MHD model. It is also possible that a prior eruption, about 14.5 hours earlier on February 12, which involved only the eastern (left) lobe of AR 11012, could have left a lingering east–west asymmetry in the energization of the configuration, which we did not attempt to reproduce here.

Looking at the physical variables in the simulation, we find the evolution is consistent with a large-scale fast-mode MHD wave launched in the corona by the expanding CME. This is illustrated in Figure 4 and the corresponding animation, which shows the evolution of the relevant magnetic flux systems from the STEREO-A plane of sky along with an overlay of negative values of the velocity divergence, $-\nabla \cdot \mathbf{v}$. Here, the outer shell of $-\nabla \cdot \mathbf{v}$ (compression) follows closely with the outer EUV front, consistent with a wavelike behavior, while the erupting flux system (gold lines) occupies a much smaller portion of the coronal volume. The wave itself is driven by the impulsive

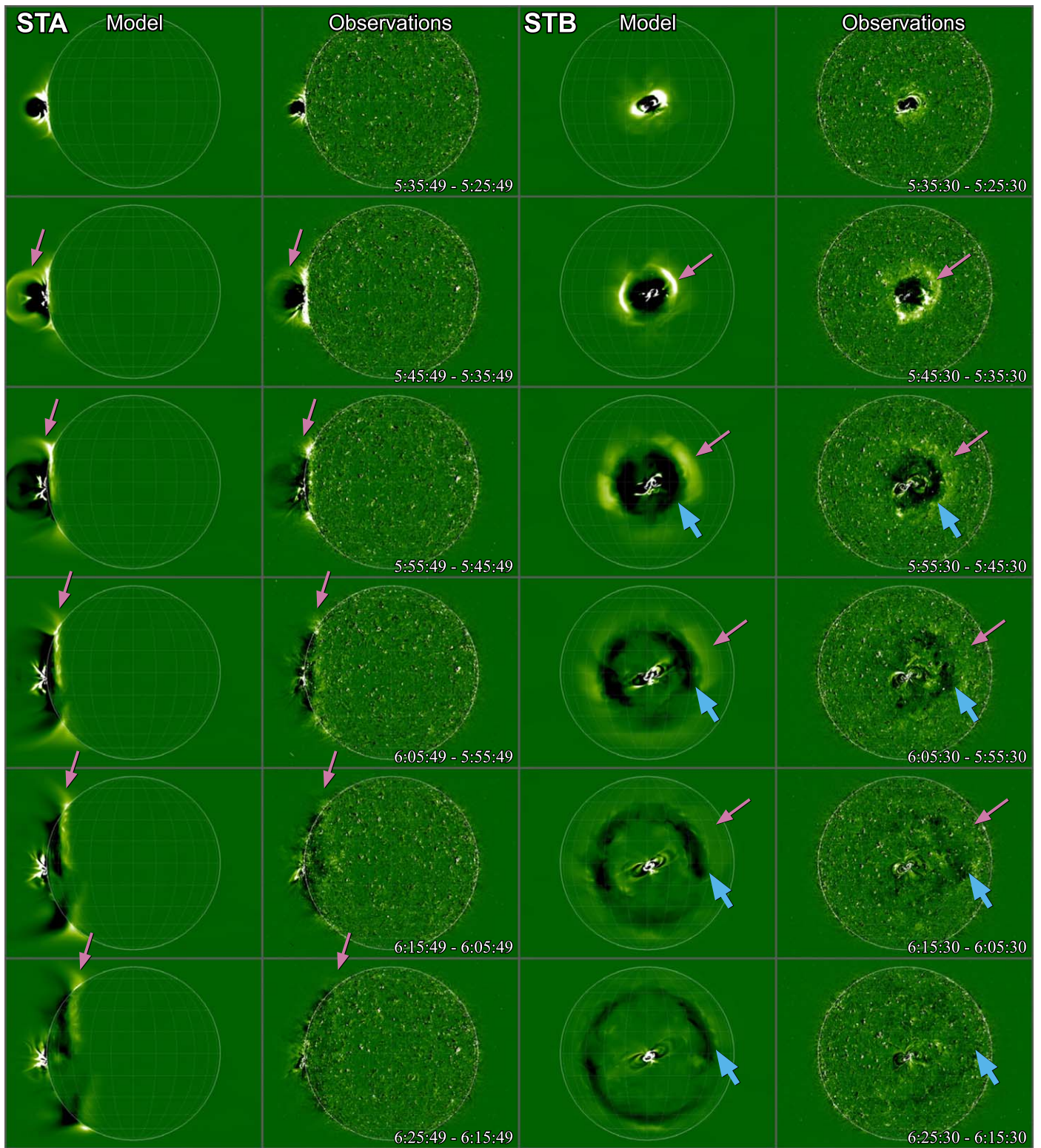


Figure 3. 10 minute EUVI 195 Å running difference images, comparing the simulated wave to observations for STEREO-A (left columns) and STEREO-B (right columns). Regions of interest are marked with arrows. Thin light magenta arrows indicate the outermost part of the apparent wave signal while the thick cyan arrows mark the extent of the trailing negative perturbation on disk in STB. The arrow locations, image cadence, and image scaling are the same for both model and observations. An animation for this figure is available. Lasting 6 s in real time, we animate the 10 minute running difference images between 05:15 UT and 06:45 UT. The frames are played forwards, backwards, and forwards again in time, first for STEREO-A and then for STEREO-B. As in the figure, the simulated wave observables are on the left and the observations are on the right.

(An animation of this figure is available.)

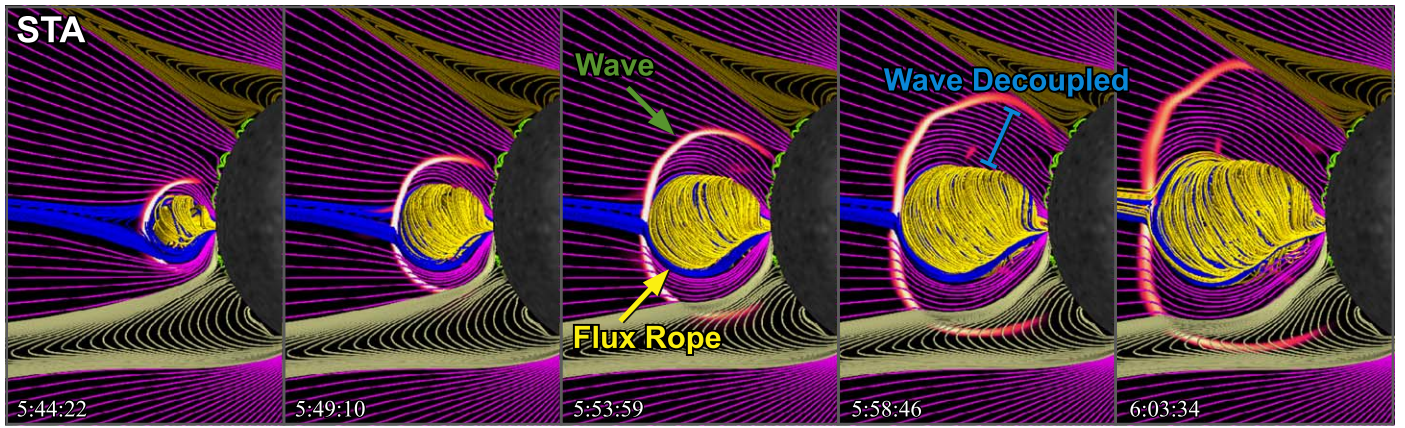


Figure 4. View of the simulated evolution at 4 minutes 48 s cadence from STEREO-A’s perspective. The field lines are overlaid with a semi-transparent contour of negative $\nabla \cdot \mathbf{v}$ in the plane of the sky, indicating the front of the large-scale wave (orange/white front). The field line colors illustrate distinct magnetic regions, including open field lines (magenta), the erupting flux rope (gold), and the closed field overlying the eruptive AR (dark blue). As indicated by the annotations, the large-scale wave decouples from the erupting flux rope in the transverse directions relatively early on in the simulation. An animation of this figure is available. The animation begins at 04:56:47 and ends at 06:44:22 UT, showing all 270 snapshots of the model at 24 s cadence. The real-time duration of the video is 9 s.

(An animation of this figure is available.)

expansion of this system during the abrupt onset of the event, and the wave decouples from the CME in the transverse directions shortly thereafter (for the basic physics of such a process; see, e.g., Vrřnak et al. 2016).

Although it is beyond the scope of this work, it is worth briefly mentioning the interaction of the wave with the streamers and coronal holes to the north and south. Visible in the later frames of Figure 4 as well as the animations of observables discussed later (Figures 9, 10, and 11) we see the simulated wave pass through the streamers to the north and south, eventually encountering the polar coronal holes, exhibiting changes in its speed and shape. Both interfaces represent a sharp change in the local fast-mode phase speed and are natural sites for wave reflection and refraction. This is consistent with previous modeling work (e.g., Schmidt & Ofman 2010 and more recently Piantshitsch et al. 2017, 2018a, 2018b) and observations of phase speed changes and reflection (e.g., Long et al. 2008; Veronig et al. 2008; Gopalswamy et al. 2009; Olmedo et al. 2012; Kienreich et al. 2013; Liu et al. 2018). The streamer disturbance also resembles the large-scale rarefaction and interaction with an EUV wave described by Kwon et al. (2013). Although quite interesting, we refer the reader to the review by Patsourakos & Vourlidas (2012) for a more detailed discussion on this topic.

3. Wave Kinematics and Perturbation Profile Evolution

3.1. Kinematics from Visually Determined Wave Fronts

The most common method for deriving the kinematics of coronal waves is to visually determine the leading edge of the wave front and to measure its distance from a radiant point. We now apply this method to the observed and synthesized EUV images. Figure 5 shows the sectors in which the wave kinematics were measured. In Figure 6, we compare distances d (top panels) and speeds v (bottom panels) of the observed (left column) and simulated wave (right column) as seen from STEREO-B (top row; on-disk view). The distances were measured along great circles on the solar surface originating from a radiant point obtained from a fit of the earliest wave front. Running difference images were used to visually determine the leading edge of the wave front. Here, we have

combined observations at 171 Å and 195 Å, because these are the only wavelengths where EUVI has provided an adequate cadence. For a meaningful comparison, we have considered only the time interval in which wave fronts were detected in the actual observations, and we have selected synthesized frames according to the cadence of EUVI. The distances were fitted both with a second-degree polynomial and a power law. Also shown is the mean acceleration a given by the polynomial fit, the power-law index δ , and the mean speed v_{lin} given by a linear fit of d .

In the observed wave, the fronts seen at 171 Å and 195 Å lie on the same kinematic curve. The wave shows a very slight deceleration but is basically consistent with a constant speed of $v_{\text{lin}} = 232 \pm 6 \text{ km s}^{-1}$. This is in good agreement with previous measurements of this event (e.g., Kienreich et al. 2009; Patsourakos & Vourlidas 2009; Warmuth & Mann 2011; Muhr et al. 2011; Podladchikova et al. 2019). The simulated wave shows the same kinematical characteristics as the observed one, with a mean speed that is only 6% lower than the observed one. Closer inspection of the speeds shows a slight acceleration in the early phase (5:38–5:50 UT) of the simulated wave, which to a lesser degree is also seen in the observations. In the simulation, the 171 Å fronts could be traced to larger distances than in the observation, and to avoid any resulting bias, we have redone the fits using only the 195 Å distance for the observed and simulated waves. The resulting kinematical parameters are summarized in Table 1, together with the parameters given by the combined 171 Å and 195 Å fronts. The simulated 195 Å kinematics are also consistent with observations: both show a very slight deceleration, and the simulated wave is $\approx 10\%$ slower than the observed one.

We now consider the kinematics of the wave as seen on the limb with STEREO-A, which is shown in the bottom row of Figure 6. In contrast to the on-disk view, we now measure the distance of the leading edge along off-limb circular paths in the height range of $1.05\text{--}1.1 R_{\odot}$ (see Figure 5). The derived kinematic parameters are also listed in Table 1. The kinematics of the observed on-disk wave are reproduced by the limb perspective: a very slight deceleration is seen, and the mean speed of $v_{\text{lin}} = 229 \pm 2 \text{ km s}^{-1}$ is equal to the speed of the on-disk wave within the margin of error. The synthesized limb

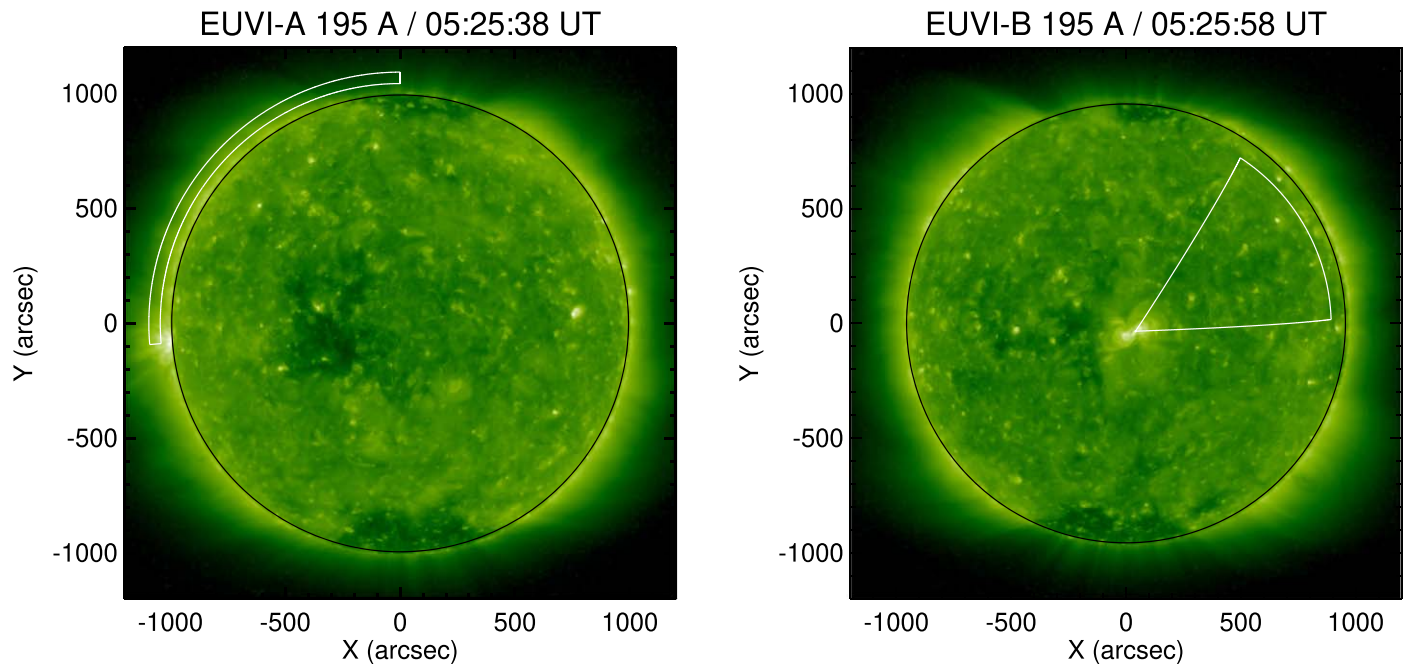


Figure 5. EUVI images showing the areas in which the wave kinematics were measured. Left: limb view of the wave with EUVI-A, where an above-the-limb circular segment is considered in the plane of the sky. Right: on-disk view of the wave with EUVI-B, where a segment defined by great circles on the solar surface is considered.

wave images yield a very slight acceleration and a mean speed that is 5% higher than the observed one. Note that while the synthesized 171 Å wave fronts could again be traced to larger distances, it was not possible to identify them at small distances, in contrast to the observations. Considering just the 195 Å images has only a weak influence on the results.

We have thus verified that the kinematics of the observed leading edge of the wave fronts is very well reproduced by the simulation (typically at the 5% level when considering the mean wave speed). Additionally, we have shown that the kinematics given by the on-disk and limb views are consistent, which reflects the fairly isotropic expansion of the wave.

3.2. Wave Kinematics from Intensity Profiles

The second main method for determining coronal wave kinematics is based on obtaining intensity profiles along a certain direction or over an angular segment (which is then averaged over the angle). The 1D intensity profiles as a function of time are often visualized as intensity stack plots (e.g., Veronig et al. 2011). Often, intensity pulses associated with the wave fronts are fitted with Gaussians, yielding the distance d of the peak of the Gaussian from the origin, as well as the width and amplitude of the Gaussian (e.g., Kienreich et al. 2011; Muhr et al. 2011). Profile analysis has been employed in many previous studies of coronal waves (e.g., Warmuth et al. 2001; Podladchikova & Berghmans 2005; Muhr et al. 2010; Veronig et al. 2010) but its use is increasing thanks to the availability of high-cadence EUV imaging with SDO/AIA (e.g., Liu et al. 2010; Long et al. 2014), where it is generally infeasible to visually identify the large number of wave fronts that result from subminute cadences.

After having established that the images obtained at different wavelengths yield consistent kinematics (see Section 3.1), we now consider only the 195 Å data. Because we have also shown that the simulation reproduces the observed kinematics

very well, we now discard the requirement of only considering simulated images at the actual observing cadence of EUVI and use the full cadence (24 s) of the simulation.

The top row of Figure 7 shows stack plots of intensity ratio profiles (which are normalized to a pre-event image) obtained from the simulated 195 Å images from the viewpoint of both STEREO-B (left column) and STEREO-A (right column). The profiles were averaged over the same sector that was used to measure the kinematics of the visually determined wave fronts in Section 3.1. The bright lane moving from small to large distances corresponds to the propagating wave front. Each profile was fitted with a Gaussian, yielding the distance, d , of the wave peak from the radiant point as indicated by black dots in the kinematics plots on the bottom row of Figure 7. The fits also provide the peak intensity ratio (i.e., amplitude), and the FWHM width of the wave front, which are discussed in Section 3.3.

The distances and speeds of the wave peak as given by the Gaussian fits are plotted in the bottom row of Figure 7 as a function of time. As in Section 3.1, we have fitted the distances with a second-degree polynomial and a power law. Here, we do not use the distances measured before the time of the first observed wave front (these data points are shown in gray in the bottom row of Figure 7). The resulting kinematics of the wave peak are basically consistent with the visually determined leading edge, namely, a very slight deceleration. The mean speed of $v_{\text{lin}} = 193 \pm 1 \text{ km s}^{-1}$ is $\approx 10\%$ lower than the one of the visually determined leading edge of the simulated wave. However, it is clearly evident that the speed evolution is more complex than reflected by the simple fits. We note a very low apparent wave speed in the early phase ($v \approx 100 \text{ km s}^{-1}$ up to 5:43 UT), after which the speed rapidly rises to nearly 300 km s^{-1} . After this peak, the wave speed decreases to about 200 km s^{-1} and remains at this level until the wave can no longer be tracked.

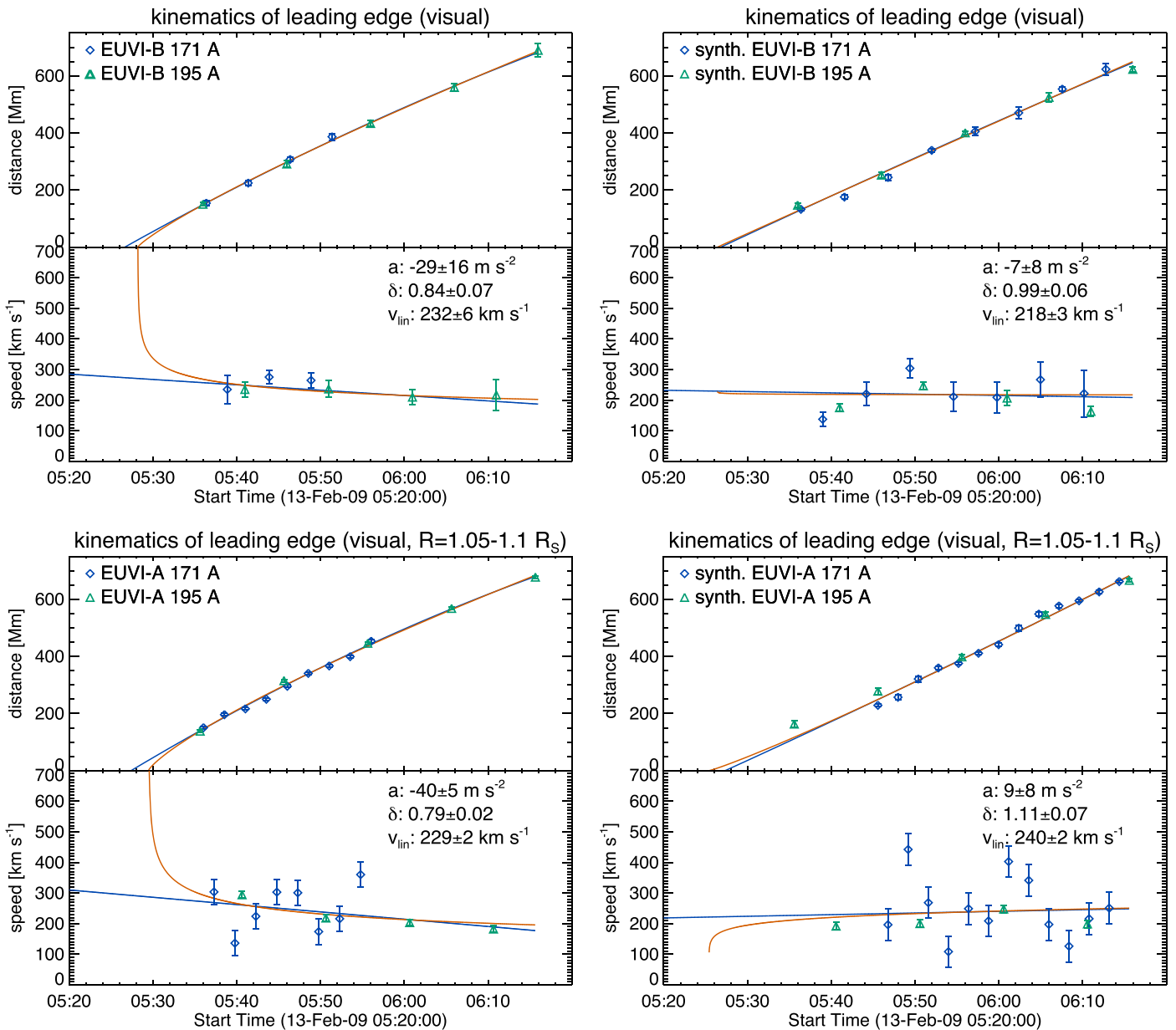


Figure 6. Top row: kinematics of the coronal wave as seen on the solar disk with STEREO-B/EUVI (left) and as simulated (right). Bottom row: kinematics of the coronal wave as seen on the solar limb with STEREO-A/EUVI (left) and as simulated (right). The plots show the distance d of the leading edge of the wave front (determined visually) from the extrapolated radiant point (upper panels of the plots), and the corresponding speeds v (lower panels), both as a function of time t . Also shown are second-degree polynomial (blue line) and power-law fits (orange line), and the corresponding mean acceleration a , the power-law index δ , and the mean speed v_{lin} is indicated.

For comparison, the distances and speeds of the wave peak derived from the observed profiles are shown in the bottom row of Figure 7 as orange circles. The mean speed is equal to the one given by the simulation. In addition, blue triangles indicate distances and speeds of the visually determined leading edges given by the EUVI-B 195 Å observations.

It is not surprising to find slightly different mean speeds for the wave peak and leading edge, given that these are physically distinct parts of the wave and that two different measurement techniques were used. We thus obtain the kinematics of a proxy for the leading edge by adding to the distance of the peak of the Gaussian half of its FWHM. This results in distances that are in reasonable agreement with the distances of the visually determined leading edges. The kinematical parameters of the wave peak and leading edge are listed in Table 1 for both

observed and simulated waves. From this, we see that the mean simulated wave speed using this technique ($v_{\text{lin}} = 213 \pm 1 \text{ km s}^{-1}$) is in good agreement with the visually determined speed.

A stack plot of intensity ratio profiles obtained from the synthesized EUVI-A 195 Å images is shown in the right-hand column of Figure 7, and again, the wave is clearly evident. The distances and speeds of the Gaussian peak as a function of time are plotted in the bottom-right panel of Figure 7. Similar to what is seen in the on-disk view, the apparent wave speed is very low initially ($v < 100 \text{ km s}^{-1}$), then it rapidly rises to $v \approx 300 \text{ km s}^{-1}$, and then oscillates predominantly in the range of $200\text{--}250 \text{ km s}^{-1}$. There are some brief episodes of higher speeds, the most pronounced one around 6:02 UT. We discuss this aspect in Section 3.3.

Table 1
Kinematics Derived from Observed and Synthesized Images Using Different Techniques

Instrument	Technique	Passband	Data	a (m s^{-2})	δ	v_{lin} (km s^{-1})
EUVI-B	Visual identification	171 & 195 Å	obs.	-29 ± 16	0.84 ± 0.07	232 ± 6
			synth.	-7 ± 8	0.99 ± 0.06	218 ± 3
		195 Å	obs.	-17 ± 20	0.89 ± 0.11	229 ± 6
			synth.	-16 ± 11	0.9 ± 0.06	202 ± 5
EUVI-A	Visual identification	171 & 195 Å	obs.	-40 ± 5	0.79 ± 0.02	229 ± 2
			synth.	9 ± 8	1.11 ± 0.07	240 ± 2
		195 Å	obs.	-57 ± 7	0.69 ± 0.02	222 ± 2
			synth.	11 ± 11	1.12 ± 0.13	214 ± 4
EUVI-B	Gaussian fit	195 Å, peak	obs.	5 ± 15	1.02 ± 0.13	193 ± 4
			synth.	-7 ± 2	0.94 ± 0.02	193 ± 1
		195 Å, leading edge	obs.	-25 ± 15	0.81 ± 0.09	192 ± 4
			synth.	-9 ± 2	0.93 ± 0.02	213 ± 1
EUVI-A	Gaussian fit	195 Å, peak	obs.	-54 ± 14	0.73 ± 0.06	193 ± 3
			synth.	-10 ± 1	0.94 ± 0.01	220 ± 1
		195 Å, leading edge	obs.	-132 ± 14	0.55 ± 0.04	212 ± 3
			synth.	-12 ± 1	0.91 ± 0.01	229 ± 1

The fits of the distances again yield a slight deceleration. The mean speed of $v_{\text{lin}} = 220 \pm 1 \text{ km s}^{-1}$ is in good agreement with the values given by the observed visual wave fronts (shown as blue triangles in the bottom row of Figure 7). The observed profiles (orange circles) yield a slightly stronger deceleration and a lower mean speed. This mainly results from the last two observed profiles, which are very irregular and ill defined. When we add half the FWHM width of the wave to the distances to get a proxy for the leading edge, the results for the simulation do not change significantly, while we obtain an even stronger deceleration for the observations in that case. Again, this is most probably an artifact of the ill-defined observed wave fronts. The kinematic parameters of all these scenarios are listed in Table 1 for reference.

We conclude that the profile method is consistent with the visual method in terms of kinematics. For the simulation, the profile method yields almost exactly the same results, while the difference is more pronounced when using the actual observations. This is most probably due to weak and irregular wave fronts late in the event.

3.3. Wave Speeds and Perturbation Profile Evolution Compared to Local Magnetosonic Speed

After having studied wave-front distances as a function of time, we now consider wave parameters as a function of distance. Figure 8 shows the wave speed v , peak intensity ratio I/I_0 , and FWHM width w as given by the Gaussian fits to the profiles obtained from the synthesized EUVI-B images. We compare the speed of the wave peak with the magnetosonic speed v_{ms} given by the model and averaged over the height range of $R = 1.05\text{--}1.1 R_{\odot}$ (shown by the turquoise line). Here we define the magnetosonic speed as $v_{\text{ms}} = \sqrt{v_A^2 + c_s^2}$, where v_A and c_s are the local Alfvén and sound speeds, respectively. As we move away from the active region, v_{ms} is decreasing from over 400 km s^{-1} to about 200 km s^{-1} . Apart from the early phase, the wave speed is close to the local magnetosonic speed. When we disregard the data points before the first observed wave front (as was done for the fits in the previous section), the mean difference between wave speed and v_{ms} is below 10%.

During the very early phase, the apparent speed of the perturbation is significantly lower than the magnetosonic speed (and indeed even lower than the sound speed), which suggests that we do not track the actual wave here, but rather the expanding CME flank. This piston generates the wave which then detaches from it (at around $d \approx 170 \text{ Mm}$ and 5:43 UT) and subsequently propagates freely (e.g., Patsourakos & Vourlidas 2009; Kienreich et al. 2009; Ma et al. 2011; Vršnak et al. 2016).

In order to investigate the relation between wave propagation speed v and local magnetosonic speed v_{ms} more quantitatively, we obtain the magnetosonic Mach number via $M_{\text{ms}} = v/v_{\text{ms}}$. Using the speeds derived from the peaks of the Gaussian fits of the simulated wave fronts and omitting the early phase of very low speeds as well as the late phase for STEREO-A (see discussion below), we obtain mean Mach numbers of $M_{\text{ms}} \approx 1.1$ for both STEREO-A and -B. Note that these numbers are consistent with the Mach numbers derived by Muhr et al. (2011) for this event. Despite fluctuations, there is a general trend of M_{ms} to decrease with distance. When we consider the early wave propagation in STEREO-B over a distance range of 230 Mm, we obtain a mean of $M_{\text{ms}} = 1.27 \pm 0.15$. Conversely, the later part of wave propagation, averaged over 400 Mm, yields a significantly lower Mach number, $M_{\text{ms}} = 1.04 \pm 0.12$. This behavior is consistent with an initially weakly nonlinear wave that decays into an ordinary linear wave. Once the wave is linear, its speed is consistent with the local magnetosonic speed. For comparison, the corresponding early and late Mach numbers for STEREO-A are $M_{\text{ms}} = 1.13 \pm 0.34$ and $M_{\text{ms}} = 1.05 \pm 0.29$, respectively. Here the behavior is less pronounced than for STEREO-B and the small-scale variation of M_{ms} is larger, but the general behavior is the same.

The agreement of wave-front speeds with the magnetosonic speed (at least during the later phase of wave propagation) has two important implications. First, it provides strong evidence that the observed coronal disturbance is truly a fast-mode MHD wave; because the magnetic field is primarily radial in the quiet corona (at least away from large-scale polarity inversion lines) and the wave propagates laterally, the fast-mode speed effectively reduces to the magnetosonic speed in this scenario. Second, both the profile method and the visual method yield

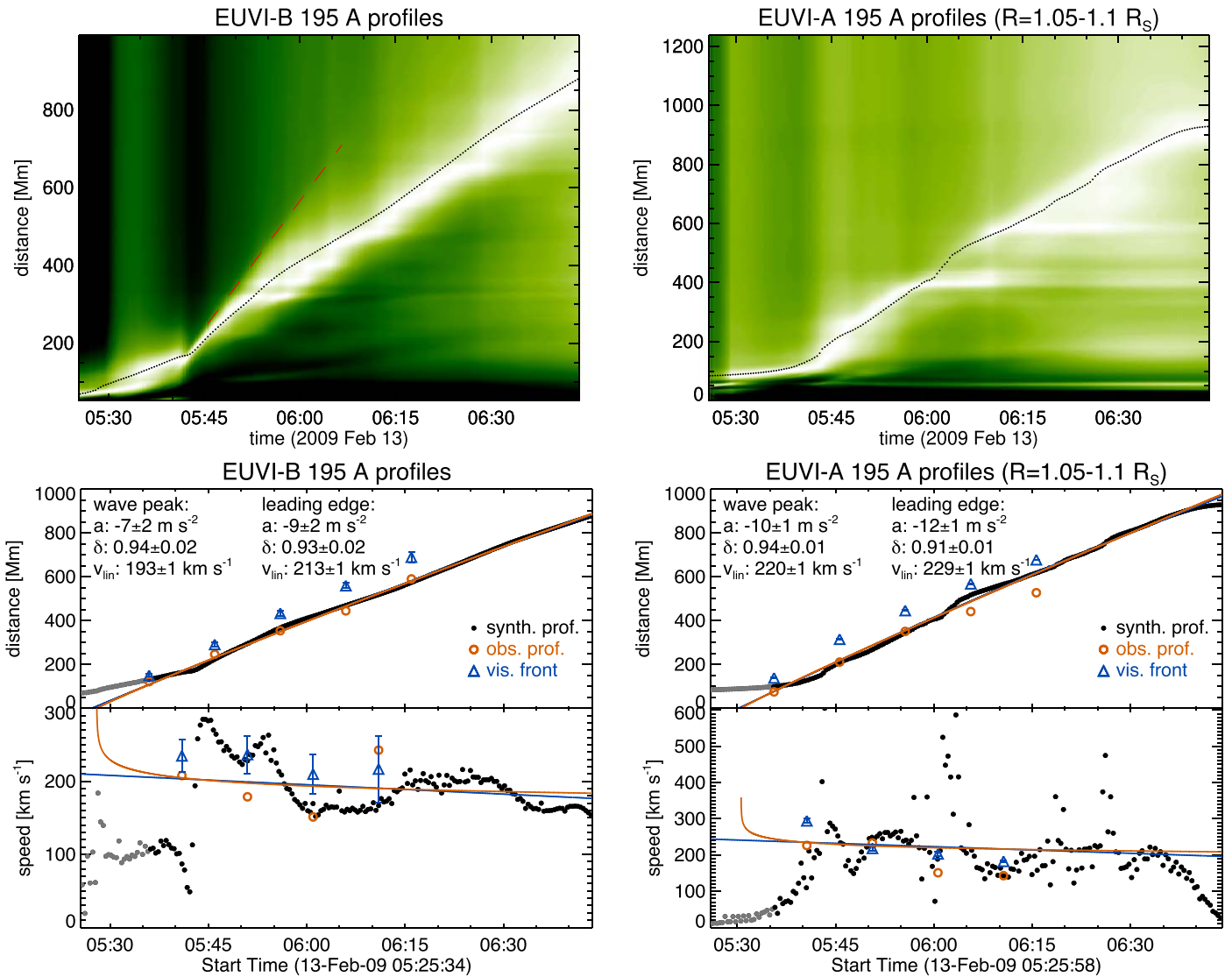


Figure 7. The top row shows, on the left, the on-disk (right, limb) view spacetime plots obtained from the synthesized EUVI-B (EUVI-A) images in the 195 Å passband. Each panel shows the intensity ratio profiles normalized to a pre-event profile, with black dots tracing the maximum of a Gaussian fit to the profiles and a red dashed line highlighting an apparent faster wave front propagating ahead of the main perturbation. This apparently faster wave front actually results from a projection effect (see discussion in the main text). The bottom row shows the kinematics of the waves derived from Gaussian fits to the intensity ratio profiles shown in the top row. Black and gray dots refer to the profiles obtained from the synthesized images and orange circles to the profiles from the observed images. The upper panels show distances derived from the maximum of the Gaussians (i.e., wave peak). Additionally, the blue triangles show the distances obtained from the visually determined leading edge of the wave fronts in the observed images. The lower panels show the corresponding speeds. Also shown are the second-degree polynomial (blue line) and power-law fits (orange line). The deceleration a , power-law index δ , and mean speed v_{lin} are given for the wave peak and the leading edge (see main text).

speeds that reflect the local fast-mode speed. This validates both kinematic analysis methods.

During the early phase of the simulated wave, however, the measured speed is several times lower than v_{ms} , which cannot be understood in terms of a fast-mode wave. It is likely that the bright feature tracked in the early phase corresponds to the erupting and overexpanding flux rope (a so-called CME bubble; see, e.g., Patsourakos et al. 2010a, 2010b; Veronig et al. 2018) that piles up plasma and ultimately launches a fast-mode wave.

The evolution of the wave’s intensity excess supports the fast-mode wave scenario (middle panel in Figure 8). In the early phase, the amplitude increases rapidly. It peaks once the apparent speed reaches its maximum, i.e., at the time when the wave is launched or becomes decoupled from the CME bubble. After the peak, the amplitude smoothly

decreases. The wave speed is larger than the magnetosonic speed when the intensity excess is large ($I/I_0 \geq 1.4$ in the distance range of 200–400 Mm), which is consistent with a (weakly) nonlinear fast-mode wave. In these so-called simple waves (e.g., Mann 1995; Warmuth et al. 2004a; Lulić et al. 2013), the propagation speed depends on the wave’s amplitude. Note that the observed intensity excess is roughly half as large as the simulated excess.

The bottom panel of Figure 8 shows that the simulated waves’ FWHM width increases with distance, which is also consistent with a nonlinear simple wave. This is in agreement with the behavior of the observed FWHM, at least for the initial to midstage of the evolution. At later stages, the observed FWHM drops while the simulated one does not. This could be attributed to the increase of noise and related uncertainties as the wave fades, and it becomes hard to detect the true width of

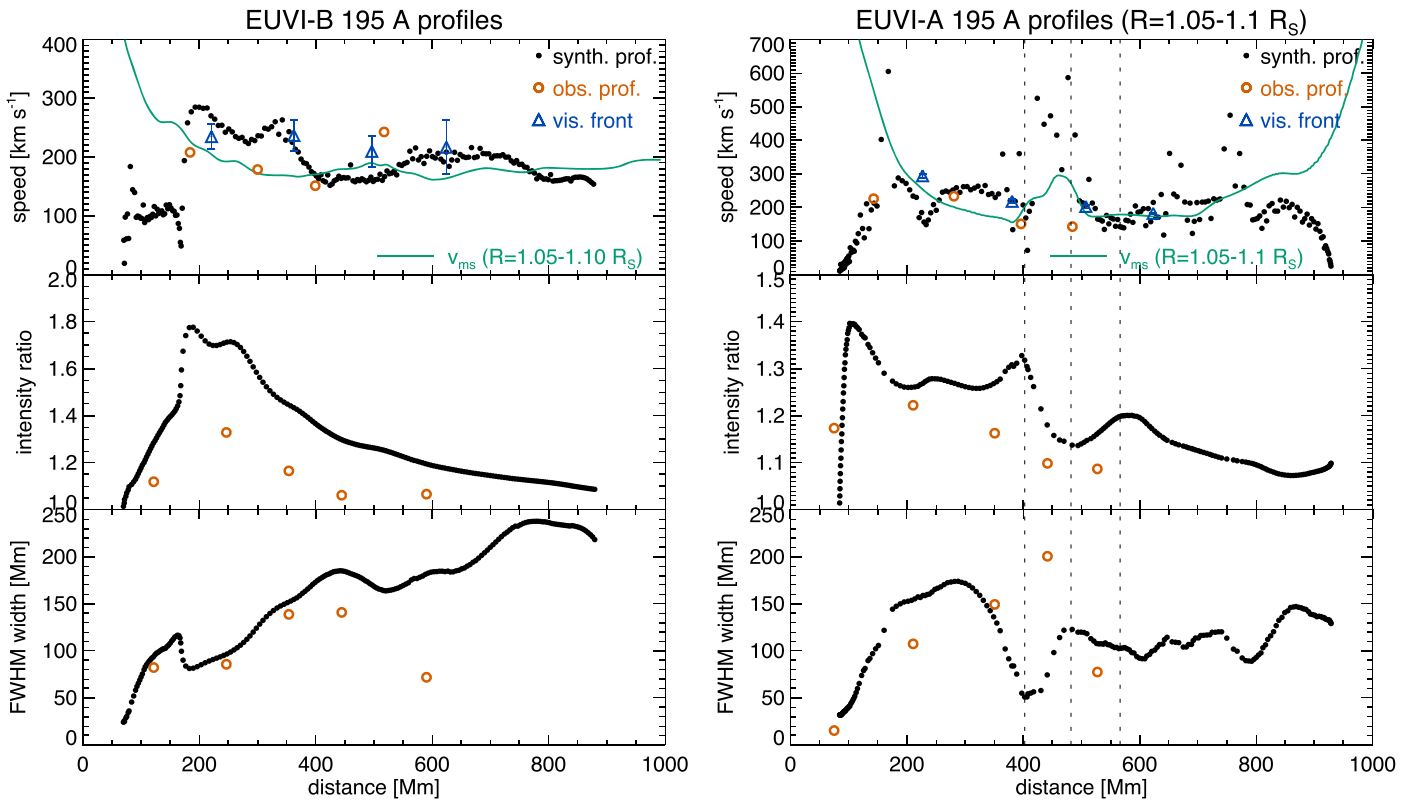


Figure 8. Kinematics and profile evolution of the wave as a function of distance, derived from Gaussian fits to the intensity ratio profiles shown in Figure 7 (left column: STEREO-B/EUVI, 195 Å, on-disk view; right column: STEREO-A/EUVI 195 Å, limb view). Black dots refer to the profiles obtained from the synthesized images and orange circles to the profiles from the observed images. The top panels show speeds derived from the maximum of the Gaussians (i.e., wave peak). Additionally, the blue triangles show the speeds obtained from the visually determined leading edge of the wave fronts in the observed images. The turquoise line shows the magnetosonic speed as given by the model averaged over the height range of $R = 1.05\text{--}1.1 R_{\odot}$. The middle row shows the peak intensity ratios derived from the maximum of the fitted Gaussians, and the bottom row shows the FWHM width of the observed pulse. The three vertical dotted lines in the right-hand column highlight the response of the wave to a local maximum of the magnetosonic speed (see discussion in the main text).

the wave over the background. We would also expect differences in the profile shape to accumulate with time, as local phase speed errors between the model and the true coronal volume will progressively lead to differing wave-front trajectories between simulation and reality.

The evolution of v , I/I_0 , and w as derived from the STEREO-A viewpoint is plotted in the right-hand column of Figure 8. Generally, the behavior of the wave is consistent with the on-disk view. Initially, the disturbance accelerates from very low speeds up to v_{ms} (again, v_{ms} is averaged over the height range of $R = 1.05\text{--}1.1 R_{\odot}$), which is accompanied by an increase of the amplitude. Later, the wave speed remains close to the magnetosonic speed, and the amplitude decreases. Beyond $d = 800$ Mm, the apparent wave speed again drops below v_{ms} . This could be an artifact due to the interaction of the wave with the polar coronal hole.

In contrast to the on-disk view, where v_{ms} remains roughly constant outside the AR, we note a local peak of v_{ms} at $d \approx 450$ Mm. This peak has a distinct influence on the wave’s evolution, as is highlighted by the three dashed vertical lines in the right-hand column of Figure 8. As the wave encounters the peak, it accelerates, while concurrently, the intensity ratio decreases and the width increases. This can be interpreted as a consequence of the increasing magnetosonic speed encountered by the wave: as the leading part of the wave speeds up, the trailing part lags behind, leading to a widening of the perturbation profile and consequently to a decrease in amplitude (due to conservation of energy). When leaving the

peak of the ambient magnetosonic speed, the reverse process happens: the wave decelerates, the width decreases as the trailing parts catch up with the leading ones, and the amplitude consequently increases. This correlation of magnetosonic speed with propagation speed, amplitude, and width of the coronal disturbance represents compelling evidence for the interpretation as a fast-mode MHD wave.

3.4. Characterizing Projection Effects

We continue our analysis by looking at the role of projection effects in complicating the kinematic analysis for certain viewing angles. As illustrated nicely by Podladchikova et al. (2019) in their analysis of this event, the projection of the leading edge of the EUV wave dome may not always correspond to the same height with time. This may lead to incorrect (or at least ambiguous) measurements of the EUV wave speed. Physically, this effect is not surprising as the fast-mode speed will naturally change as a function of height in the corona, thus altering the local phase speed of the EUV wave front (Uchida 1968; Afanasyev & Uralov 2011; Kwon & Vourlidis 2017). This height-dependent behavior is illustrated from the STEREO-B perspective in Figure 9 by displaying isocontours of $-\nabla \cdot \mathbf{v}$ at different heights with distinct colors. These contours track the outer edge of the wave dome at each height as it expands during the event. The front at larger heights has a faster apparent motion over the disk, due to the projection of the expanding wave bubble and because the overlying

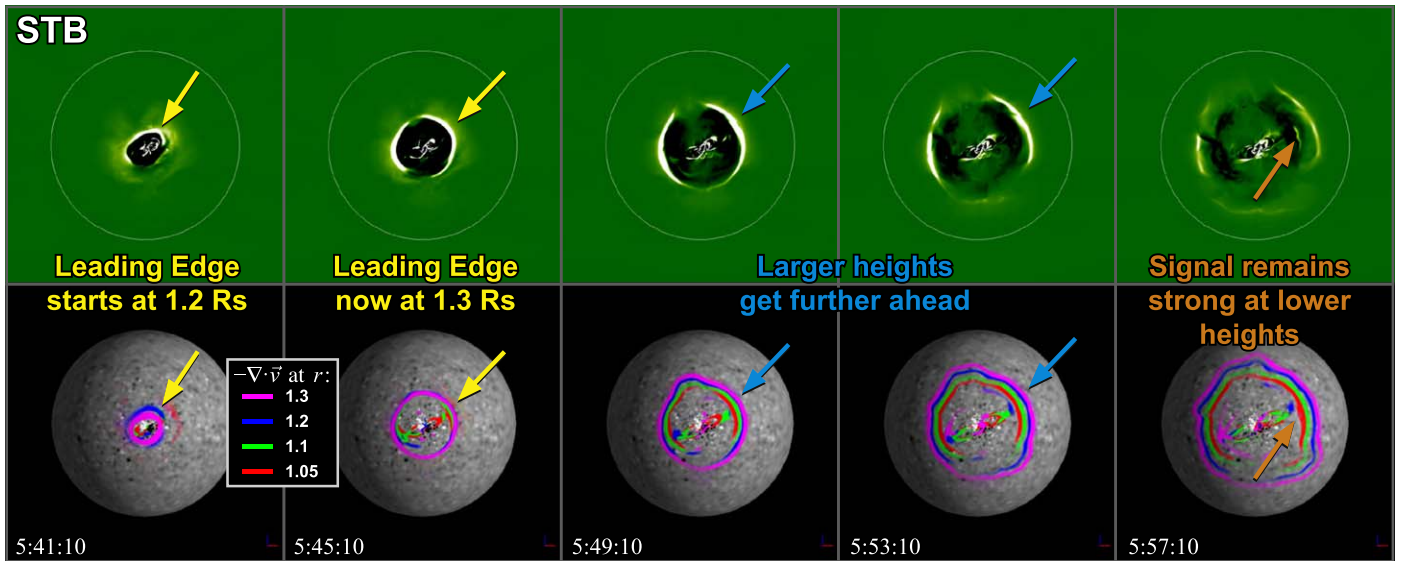


Figure 9. Analysis of the leading edge of the EUV wave for the 2009 February 13 case study simulation. The top row shows 24 s STEREO-B/EUVI 195 Å running difference images at 4 minute cadence. The bottom row shows isocontours of $-\nabla \cdot \mathbf{v}$ at four separate coronal heights. These contours indicate the local position of the wave at each height. Initially, the wave dome is just forming and the widest part in projection is $1.2 R_{\odot}$. Later, the bubble expands and the leading edge is at a higher height. Due to the emissivity dependence as a function of height, the signal remains strong at lower heights, confounding the interpretation of the apparent speed and width of the front. An animation of this figure is available. The animation begins at 04:56:47 and ends at 06:44:22 UT, showing all 270 snapshots of the model at 24 s cadence. The frames showing isocontours of $-\nabla \cdot \mathbf{v}$ are on the left and the running difference images are on the right. The real-time duration of the video is 9 s. (An animation of this figure is available.)

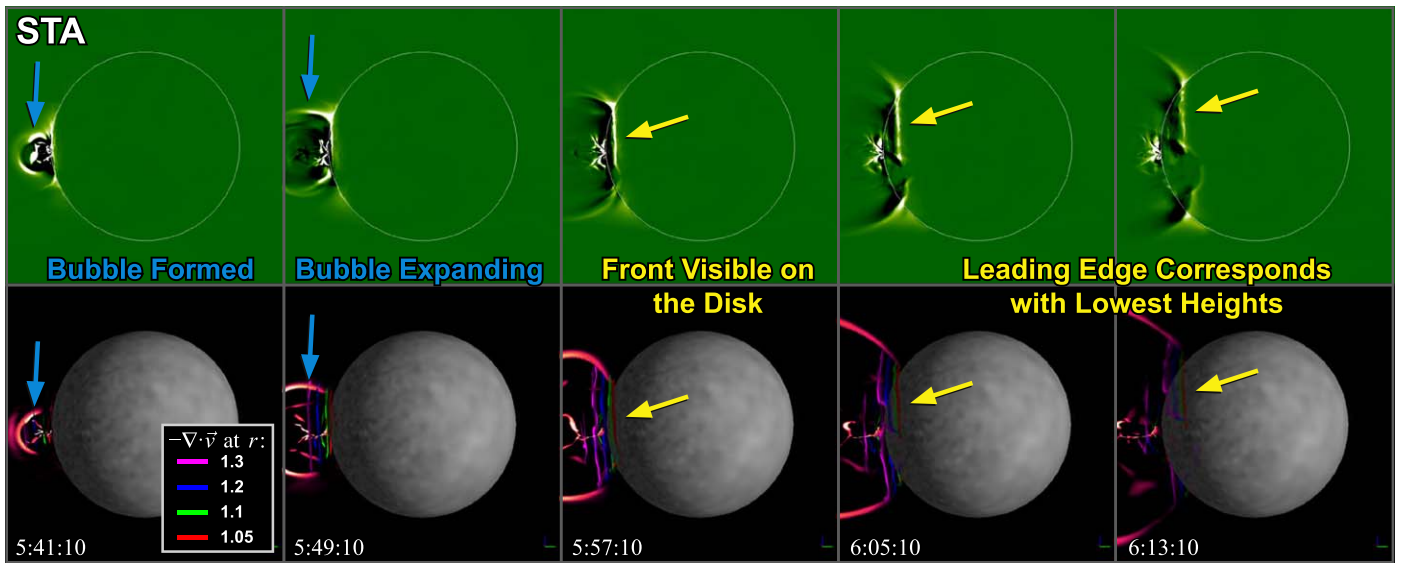


Figure 10. Same as Figure 9 but for the STEREO-A perspective (limb view) and a longer 8 minute cadence. In addition to the height isocontours, a color plot of $-\nabla \cdot \mathbf{v}$ is shown in the plane of the sky (as in Figure 4). From this perspective, the wave dome is initially seen off limb but projects onto the disk as time goes on. The leading front edge of the diffuse front corresponds to the wave at the lowest heights in the corona. This is opposite to the case of the STEREO-B perspective (disk view). An animation of this figure is available. The animation begins at 04:56:47 and ends at 06:44:22 UT, showing all 270 snapshots of the model at 24 s cadence. The frames showing isocontours of $-\nabla \cdot \mathbf{v}$ are on the left and the running difference images are on the right. The real-time duration of the video is 9 s. (An animation of this figure is available.)

Alfvén speed increases with height. This is potentially a confounding factor for some events and one that could hamper blind seismological estimates.

Figure 10 shows the same projection visualization as Figure 9 but now for the limb perspective of STEREO-A. Here we see another interesting aspect of the wave projection, because now the trend in the height of the leading front has reversed. Initially, the bubble is only visible off the limb, and the height of the wave is clear in these locations. However, as

the wave expands and projects onto the disk, we see that the lowest heights correspond to the obvious leading edge in the 195 Å running difference images. This is clearly a simple geometric effect, but it is worth pointing out because the leading edge of the diffuse front to the west in STEREO-B corresponded to about $1.3 R_{\odot}$, while for STEREO-A, it is at about $1.05 R_{\odot}$. This result is consistent with early analysis by Ma et al. (2009) and idealized modeling by Hoilijoki et al. (2013), and again emphasizes the fact that one must take care in

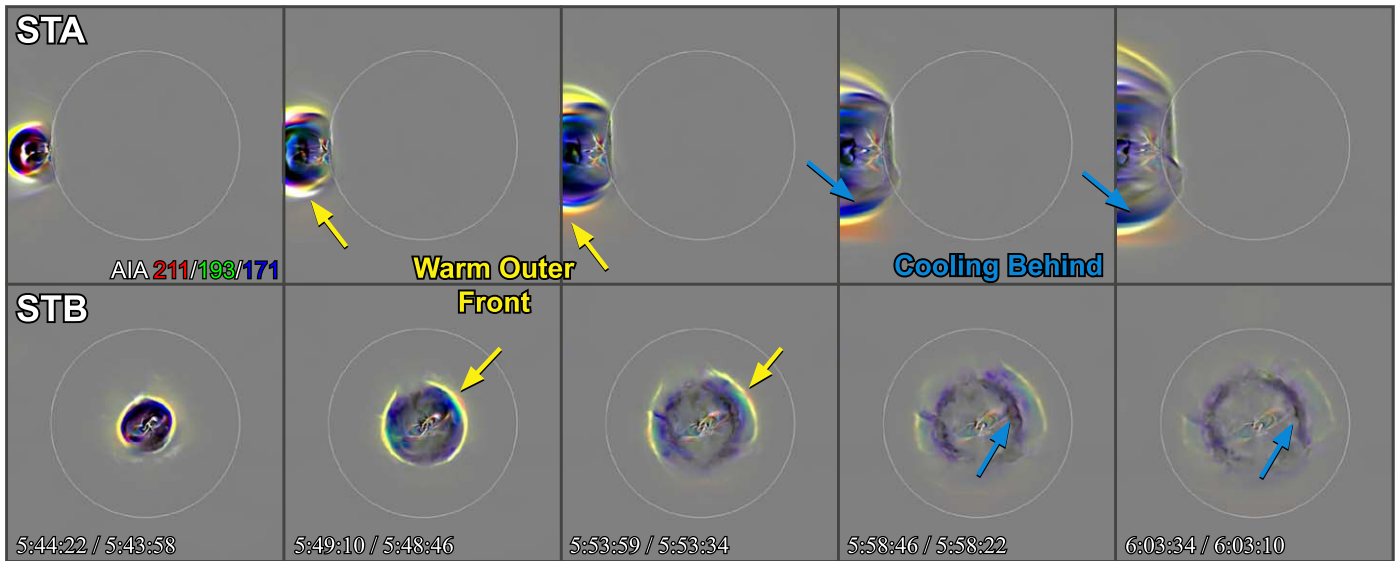


Figure 11. 24 s AIA tricolor running ratio images shown at fixed intervals during the simulated event. The RGB color channels show running ratios in the synthetic AIA 211, 193, and 171 Å images, respectively. A clear warming signal is seen in the orange-red colors (yellow arrows) followed by a cool rarefaction signal in black-blue colors (cyan arrows). These signals correspond well with the expected temperature and density changes that are present in the simulation and resemble the AIA tricolor signals for observed EUV waves. An animation of this figure is available. The animation begins at 05:15:10 and ends at 06:44:22 UT, showing 224 frames at 24 s cadence. The STEREO-A perspective is on the left, the STEREO-B perspective is on the right. The real-time duration of the video is 7 s.

(An animation of this figure is available.)

comparing the position of the waves and their eruption drivers from 3D viewpoints (e.g., Kwon et al. 2014; Lario et al. 2014).

Projection effects also manifest themselves in the intensity stack plots. Closer inspection of the stack plot derived from the STEREO-B viewpoint (see Figure 7) reveals not just the main perturbation corresponding to the wave, but additionally, a weaker emission feature ahead of it (highlighted by the red dashed line). This feature is about twice as fast as the wave itself. Without a detailed knowledge of our simulation, such a feature might have been interpreted as a second distinct wave. However, it is merely the consequence of the viewing geometry. The profiles contain contributions from different parts of the vertically extended wave front, which is viewed under an oblique angle. Because the emissivity depends on the height, the signal is strongest at low heights, corresponding to the main perturbation feature that is tracked by the profile method. The weaker emission from larger heights contributes signal to the leading part of the disturbance, leading to asymmetric profiles that give the impression of a precursor wave.

Fast weak waves have been identified in stack plots using AIA data (e.g., Chen & Wu 2011; Liu & Ofman 2014). We conjecture that at least in some of these cases, the apparent leading waves may be attributed rather to this projection effect. In particular, this could provide a reasonable explanation for the exceedingly fast waves ($v \approx 1000 \text{ km s}^{-1}$) that were reported by Nitta et al. (2013) based on intensity profiles obtained from AIA. As these speeds well exceed the local magnetosonic speed, the perturbations have to be highly nonlinear simple waves or shocks, which are expected to decelerate as their amplitude drops. This is commonly observed in Moreton waves (e.g., Warmuth et al. 2004b) and high-speed EUV waves (Warmuth & Mann 2011; Muhr et al. 2014; Long et al. 2017a), but this was not the case in the events in Nitta et al. (2013). Our simulation has shown that projection effects can generate rapidly propagating emission features in intensity

stack plots that could easily be misinterpreted as physically distinct waves.

4. Thermal Analysis

The multiple EUV passbands provided by instruments such as SDO/AIA, which simultaneously image the low solar corona at different temperatures, offer the opportunity to examine the thermal evolution of global EUV waves. The simplest approach is to combine three of the passbands from SDO/AIA, each observing different temperature plasma, and examine the evolution of the plasma during the passage of the global EUV wave using ratio or difference images. An example of this is shown in Figure 11, where we forward-model the emissivities for the 211, 193, and 171 Å passbands and use them to generate tricolor RGB running ratio images. The (broad) sensitivity of the three passbands peaks at different plasma temperatures (~ 1.8 , ~ 1.6 , and ~ 0.9 MK, respectively), so the RGB running ratios show heating in yellow-red and cooling in blue. For this simulation, it is clear from this diagnostic that the global EUV wave has a hot leading edge and is followed by a cool rarefaction signal. Such a temperature enhancement would be expected for a compressional MHD wave (as is simulated here, Section 2.4, Figure 4), and this signature is consistent with the tricolor heating/cooling behavior seen in real events (Schrijver et al. 2011; Downs et al. 2012; Liu et al. 2018). In particular, please refer to Figure 6 from Downs et al. (2012) for tricolor observations of a similar wave observed by SDO/AIA as well as their appendix for an in-depth discussion of the interpretation of tricolor ratios.

Although this approach is useful for quickly illustrating the thermal behavior of a global EUV wave event, a more detailed examination of temperature (and potentially density) evolution requires inverting the intensities of the different EUV passbands observed by SDO/AIA to derive the differential emission measure (DEM). While this is an ill-posed numerical

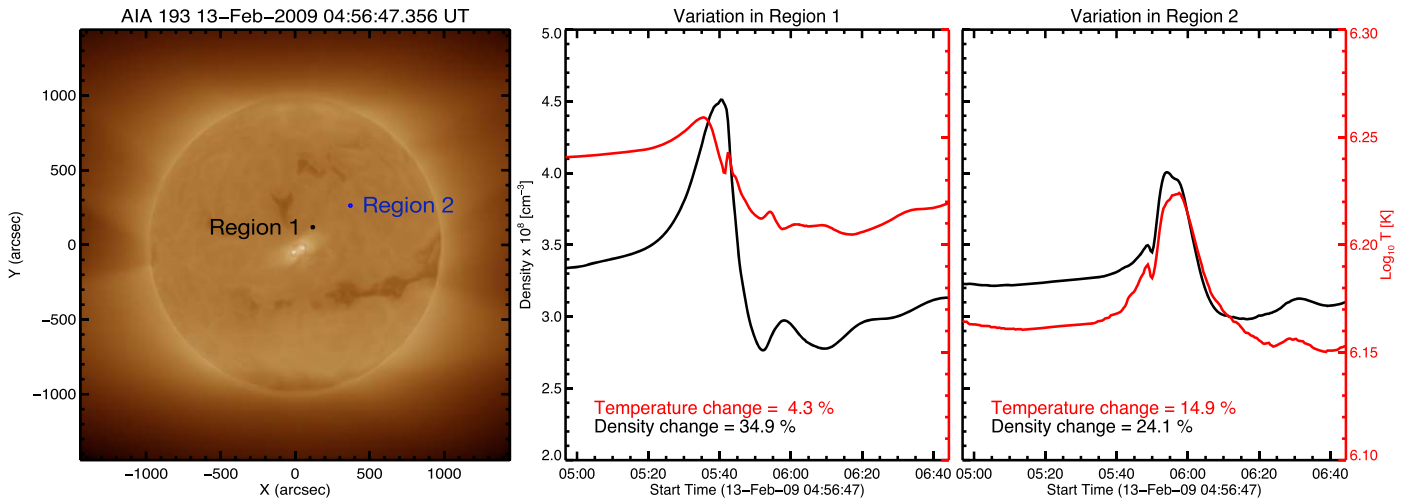


Figure 12. Left: forward-modeled 193 Å image showing the simulation near the start of the eruption. The colored boxes indicate the regions that were used to derive the average densities and temperatures from DEM inversions. Middle: the temporal variation of the DEM-inferred density and temperatures near the eruption site (Region 1, indicated by the black box, left panel). Right: the temporal variation of the same quantities for a location further away from the eruption site (Region 2, indicated by the blue box, left panel). The relative start to peak changes in density and temperature are indicated.

problem, a series of techniques have been developed, which can be used to estimate the DEM and hence infer the physical properties of the observed coronal plasma (see, e.g., Hannah & Kontar 2013; Cheung et al. 2015). The technique developed by Hannah & Kontar (2013) in particular has been used by multiple authors to examine the thermal evolution of global EUV waves and the response of the surrounding corona to the passage of a global EUV wave. Vanninathan et al. (2015) found a temperature increase of $\sim 5\%$ – 6% and a density increase of $\sim 6\%$ – 9% for a global EUV wave observed by SDO/AIA on 15 February 2011 and identified the heating to take place at the frontal part of the wave, while Long et al. (2019) found temperature (density) increases of 0.5% – 1.1% (10% – 26%) for four global EUV wave events occurring between 28–30 April 2014.

The approach taken by both Vanninathan et al. (2015) and Long et al. (2019) is to calculate the DEM using an inversion code (in these cases, the technique developed by Hannah & Kontar 2013) and then integrate the DEM over all temperature bins to get an estimate of the change in temperature in a region of quiet Sun where the global EUV wave is shown to pass through. The variation in density can then be estimated by assuming a line-of-sight length (estimated by Vanninathan et al. 2015 to be ≈ 90 Mm). This length is consistent with the height calculated for global EUV waves including the 13 February 2009 event (Kienreich et al. 2009; Patsourakos & Vourlidas 2009; Podladchikova et al. 2019) and has been subsequently used by Long et al. (2019). To enable a comparison here with Long et al. (2019) and the simple tricolor method (Figure 11), we applied the DEM inversion method of Hannah & Kontar (2013) to the synthetic AIA data to two regions, one just outside the source region and one farther away, well within the quiet Sun along the wave path. We examine the temporal variation of the DEM-inferred density and temperature for both, and the results are shown in Figure 12.

The regions of interest where we compute the DEM inversions are indicated by the black and blue boxes identified as Regions 1 and 2 in the left-hand panel of Figure 12, with the middle and right-hand panels showing the variation in density (black) and temperature (red) with time. It is clear that the

simulated wave event discussed here exhibits a very large variation inferred for density ($\sim 35\%$), with a much smaller corresponding increase inferred for temperature ($\sim 4\%$) near the eruption site. These values are consistent with observations of driven EUV waves relatively close to the source region, where the density increase resulting from the passage of a global EUV wave is much larger than the temperature increase (cf. Long et al. 2019). They are also consistent with the interpretation of a global EUV wave as a large-amplitude, nonlinear wave or driven shock, as discussed by Long et al. (2017b).

Farther from the source region, the density and perturbations are $\sim 24\%$ and $\sim 15\%$, respectively, consistent with an adiabatic process ($T\rho^{-1} = \text{Const}$) and the theoretical expectation for a simple compressional wave (as measured and discussed by Schrijver et al. 2011; Downs et al. 2012; Vanninathan et al. 2015). Of course, the combination of DEM inference, inherent wave geometry, and nonideal processes will conspire to make this signature quite complex in practice. For example, we see that values do not return to their pre-event levels at either location, again similar to Vanninathan et al. (2015).

5. Discussion and Conclusions

The physical nature of large-scale coronal waves has been debated intensively during the last two decades (e.g., Patsourakos & Vourlidas 2012; Warmuth 2015; Long et al. 2017b). Finally, we are at the position of having at our disposal both excellent observations (mainly in the form of high-cadence, multi-viewpoint EUV imaging data) and unprecedented modeling capabilities. In this paper, we have brought together these two assets. By modeling a well-studied “textbook” coronal wave (the event of 2009 February 13) that was observed by STEREO in quadrature, we have addressed several key issues that are highly relevant to our understanding of these phenomena.

5.1. Accuracy of the Simulation

A detailed comparison of the observed images and the images synthesized from the modeled wave was conducted in order to assess the accuracy of the wave modeling. Visual inspection of these images has revealed that the overall

morphology of the coronal wave is reproduced by the simulation very well. Moreover, we found that the kinematics of the modeled wave is consistent with the observations. All measurements yield a constant speed ($v \approx 200 \text{ km s}^{-1}$) or a very slight deceleration ($a \approx -30 \text{ m s}^{-2}$), with mean wave propagation speeds agreeing to better than 10%. The resulting speeds also coincide with previous independent kinematical studies of this event (Kienreich et al. 2009; Patsourakos & Vourlidas 2009; Muhr et al. 2011; Podladchikova et al. 2019). The temporal evolution of the intensity excess of the wave is also reproduced very well by the simulation; however, the amplitudes are higher than the observed ones by a factor of ≈ 2 . The wave-front width is mostly reproduced well, with a divergence from observations only late in the wave propagation. This is most probably caused by the noise in the observed data.

That said, it is important to emphasize the overarching purpose of this comparison: to establish a plausible connection between the physics described by the model and the observables through a direct comparison with data. Our goal was not to fine-tune every aspect in order to convey a superficially “perfect” result, which would be missing the point. While a solid agreement can support our approach and constrain the magnetic field strength and plasma parameters in the quiet-Sun regions that we examined, it is not proof that our choices are somehow universally correct. Keeping in mind that the modeled 3D phase speed distribution is inherently linked to our specific choice of magnetic boundary conditions and coronal heating approach (both of which have inherent limitations and uncertainties), we can only conclude that this combination worked well for our purposes¹⁰. Furthermore, while we believe aspects of the eruption methodology are innovative and useful for capturing the energized state, slow rise, rapid expansion, and flux-ejection processes (standard elements of bipolar solar eruptions, e.g., Shibata & Magara 2011), such modeling cannot preclude all possible alternative eruption cartoons or scenarios. Instead, our aim was to convey (1) how these simple physical mechanisms can give rise to remote-sensing observables that are consistent with EUV wave observations, and (2) that the analysis of these observables can, in fact, shed light on the underlying physical state and evolution of the corona.

5.2. Influence of Analysis Method on Derived Kinematical Parameters

In the study of wave kinematics, two main methods are commonly used: visual identification of the leading edge and fitting of intensity profiles. We have applied both methods to the observed and synthesized images. For the observations, the speeds derived from peaks of the Gaussian fits to the intensity profiles are $\approx 10\%$ lower than the speeds given by the visually determined leading edges. Adding the wave half-width to the Gaussian peak positions has the effect of reducing the disagreement between the two methods to $\approx 5\%$ for STEREO-A, while the disagreement is only slightly reduced for STEREO-B. Making the same comparison for the simulation, we find Gaussian peak speeds that are mostly consistent with the speeds of the leading edge. Using the Gaussian peak positions plus the wave half-width leads to

speeds that agree with the visually determined leading-edge speeds at the 5% level. We conclude that, intrinsically, both the visual and profile method yield consistent kinematics. In the case of actual observations, adding the wave half-widths to the Gaussian peak positions results in a significantly better agreement with the visually determined speeds.

5.3. Influence of Temporal Cadence

The wave was observed at temporal cadences of 2.5–5 minutes (at 171 Å) and 10 minutes (at 195 Å), while the simulation produced snapshots at a time resolution of 24 s. This allows us to study the influence of the cadence on the derived kinematics. Generally, the various cadences had no impact on the derived kinematics, which is not too surprising because the given wave event was basically moving at a constant speed. The weak deceleration of the wave was evident at all cadences, even at 10 minutes. For initially fast and strongly decelerating waves (e.g., $v > 400 \text{ km s}^{-1}$, $a < -100 \text{ m s}^{-2}$; see Warmuth & Mann 2011; Muhr et al. 2014), the effect of the cadence will naturally be more important. This applies to the general kinematics of wave propagation. However, the simulation has shown two small-scale effects on the wave speed that could not be detected in the observations due to the insufficient cadence. First, very low speeds were derived from the synthesized images during the launch phase of the wave. This is due to the fact that initially, it is not the wave itself that is being tracked but rather the expanding CME flank that acts as the piston generating the wave. This shows that studying the generation and decoupling of the wave from the driver requires imaging at a high cadence. Second, the synthesized images showed the reaction of the coronal wave to a local enhancement of the fast-mode speed, which was not seen in the observations. In summary, we have shown that a detailed analysis of wave formation and propagation requires images at the temporal cadence that is typically provided by AIA.

5.4. Influence of Line-of-sight Integration Effects

Coronal EUV waves are observed in optically thin emission, thus, the wave fronts are always seen as line-of-sight integrations that are projected onto the solar disk (or the plane of the sky when observed off limb). Therefore, projection effects influence the appearance and location of wave features (e.g., Ma et al. 2009; Dissauer et al. 2016; Podladchikova et al. 2019), which can affect the determination of kinematics. For the event studied here, the simulations have clearly shown that the projection of the wave dome onto the disk does not always correspond to the same wave-front height as a function of time. This is caused by the fast-mode speed that is increasing with height, which has the effect that higher parts of the wave front have a faster apparent motion on the disk. This leads to ambiguities in determining the leading edge of the wave front. In intensity profiles, this effect results in a more shallow intensity increase ahead of the main perturbation, which is due to higher parts of the wave front. In an intensity stack plot, this gives the impression of a faster and weaker wave moving in front of the wave proper.

The methods for deriving wave kinematics as used in this paper have been proven to be rather robust with respect to the influence of projection effects. However, this may be different in another event, for another viewing geometry, or for alternative measurement methods. Automatic methods might be particularly sensitive to projection effects. We propose that

¹⁰ See Downs et al. (2011) for an example of how wave properties may vary with the coronal field strength and eruption model.

some of the apparently very fast waves reported by studies using these techniques (e.g., Nitta et al. 2013) may actually be due to such projection effects.

5.5. Extracting Quantitative Physical Parameters

Large-scale coronal waves have been applied as diagnostic tools to extract quantitative physical parameters of the corona, such as the local magnetosonic speed. When this “global coronal seismology” is combined with information on density and temperature, it allows the derivation of the coronal magnetic field strength, a notoriously elusive yet crucial parameter (e.g., Mann et al. 1999; Warmuth & Mann 2005; Long et al. 2013; Kwon et al. 2013).

Our simulation allows us to assess whether the measurement techniques that are typically used in coronal seismology are able to accurately quantify the local fast-mode speed. We have compared the wave speeds derived from the synthesized images (using the profile method) with the magnetosonic speed given by the model. We found that the measured wave speed is significantly larger than v_{ms} during the earlier half of the wave’s propagation, which could be due to the fact that the wave is initially (weakly) nonlinear. However, during the latter half of the propagation, the measured wave speed agrees with v_{ms} to within $\approx 10\%$. Assuming that the wave is now really linear, this implies that the technique of global coronal seismology is able to quantitatively constrain the magnetosonic speed and hence the coronal magnetic field strength with an accuracy at the 10% level. Note that this is also the typical level of agreement between speeds derived with different methods or from the two orthogonal viewing angles.

Due to their transient nature, plasma diagnostics of EUV waves through spectroscopy are difficult and only rarely available (Harra et al. 2011; Veronig et al. 2011). However, SDO/AIA observations in multiple passbands at different temperatures have enabled the development of different techniques for deriving the plasma properties of the low solar corona. In particular, multiple techniques have been developed to derive the DEM of the coronal plasma and thus estimate the variation in temperature and plasma density. The regularized inversion technique developed by Hannah & Kontar (2013) was here applied to the simulated event and used to derive the evolution of the inferred temperature and density in a region where the wave passed through. It was found that the wave exhibited an increase in the inferred density and temperature, with the density increase shown to be much greater than the temperature increase near the source region, and adiabatic farther away. This behavior is consistent with observations and would be expected for a large-amplitude wave or shock near the source region that subsequently decouples from the CME driver and decreases in amplitude as it propagates. This analysis also demonstrates the ability of these inversion techniques to probe the physical behavior of these waves.

5.6. Constraining the Physical Nature of the Global EUV Wave

There has been an intense debate on the physical nature of large-scale coronal waves. Besides the interpretation as fast-mode waves or shocks (e.g., Uchida 1968; Wang 2000; Vršnak et al. 2002; Warmuth et al. 2004a; Veronig et al. 2008; Patsourakos & Vourlidis 2009; Lulić et al. 2013; Warmuth et al. 2016), different kinds of magnetic reconfiguration scenarios have been proposed that claim that these phenomena

are not actual waves in the physical sense (e.g., Attrill et al. 2007; Delannée et al. 2008). Both scenarios have also been combined (e.g., Chen et al. 2002). Recently, there has been growing consensus that the main perturbation that is usually called a coronal wave is indeed caused by a fast-mode wave that might also be nonlinear or shocked (see Warmuth 2015; Long et al. 2017b).

Assuming that this interpretation is correct, the perturbation should propagate at the local fast-mode speed in case it has a small amplitude, while it will travel faster than that in case it has a large amplitude (nonlinear wave or shock). We have found that the average speed of the simulated wave is $\approx 10\%$ higher than the local magnetosonic speed. Closer inspection has shown that the wave initially has a magnetosonic Mach number of $M_{\text{ms}} \approx 1.2$, which drops to $M_{\text{ms}} \approx 1.05$ during its propagation. This is consistent with a weakly nonlinear wave that decays into an ordinary fast-mode wave. Above, we have shown that speeds derived from the simulated wave agree to better than 10% with the speeds derived from the actual observations. Therefore, we can transfer our result from the simulation into reality and conclude that the coronal wave of 2009 February 13 is consistent with an initially weakly nonlinear fast-mode wave.









Another important argument for the wave nature of the disturbance is given by the correlated evolution of speed, amplitude, and wave-front width when inhomogeneities of the local fast-mode speed are encountered. When the wave enters a region of elevated fast-mode speed, it accelerates. Concurrently, its width increases because the leading edge now moves faster than the trailing one. At the same time, its amplitude decreases due to the conservation of energy. When the wave exits the high-speed region, the reverse process takes place. All this is clearly shown by the simulated wave.

Finally, we note that no type II burst was observed in this event, in contrast to faster coronal waves, which tend to show a high association with type II bursts (e.g., Klassen et al. 2000; Warmuth et al. 2004a; Warmuth 2010; Muhr et al. 2014; Long et al. 2017a; Veronig et al. 2018). This is not surprising because type II emission requires energetic electrons that are accelerated only by a supercritical shock, whereas the present wave was only weakly supermagnetosonic.

Overall, this work highlights an essential use of data-constrained simulations: connecting what we observe via remote sensing to the underlying physics. From such a combined analysis, we have built strong support for the interpretation of the 2009 February 13 EUV wave as a dome-shaped fast-mode wave. This wave was weakly nonlinear initially and launched due to an erupting and expanding flux rope that acted as a temporary 3D piston. This evolution was accurately modeled in the framework of a 3D thermodynamic MHD simulation, and the observational relevance of the simulation was established via forward-modeling. Furthermore, by demonstrating how the wave kinematics and perturbation profiles can in fact infer local speeds and plasma properties, we provide essential validation and context for some commonly used observational techniques. This result is quite encouraging but also emphasizes the importance of taking care in the analysis, paying heed to the inhomogeneous corona and inherent geometry of the evolving, dome-shaped EUV wave front.

The authors thank the International Space Science Institute (Bern, Switzerland; <https://www.issibern.ch>) for supporting the International Working Team on “The Nature of Coronal Bright Fronts” led by D. M. Long and D. S. Bloomfield. We also thank the anonymous reviewer, whose insightful comments helped improve the manuscript. C.D. was supported by the NASA Living With a Star (NNX14AJ49G) and Heliophysics Supporting Research programs (NNX14AH70G). A.W. was supported by the German Space Agency DLR under grant No. 50 QL 0001. D.M.L. received funding from the European Community’s Seventh Framework Programme under grant agreement No.284461 (eHEROES project). D.M.L. also acknowledges support from the European Commission’s H2020 Programme under the following grant agreements: GREST (no. 653982) and Pre-EST (no. 739500), support from the Leverhulme Trust for an Early-Career Fellowship (ECF-2014-792), and is grateful to the Science Technology and Facilities Council for the award of an Ernest Rutherford Fellowship (ST/R003246/1). D.S.B. received funding from the European Union’s Horizon 2020 research and innovation program under grant agreement No.640216 (FLARECAST project). R.-Y.K. acknowledges support from the National Research Foundation of Korea (NRF-2019R1F1A1062079) grant funded by the Korean government (MSIT; Project No. 2019-2-850-09). A.M.V. acknowledges funding by the Austrian Space Applications Programme of the Austrian Research Promotion Agency FFG (ASAP-11 4900217, ASAP-14 865972) and the Austrian Science Fund FWF (P24092-N16). A.V. acknowledges support from NASA grants 80NSSC19K1261 and 80NSSC19K0069. B.V. received funding from the Croatian Science Foundation under projects 6212 “Solar and Stellar Variability” and 7549 “Millimeter and Submillimeter Observations of the Solar Chromosphere with ALMA”.

ORCID iDs

Cooper Downs  <https://orcid.org/0000-0003-1759-4354>
 Alexander Warmuth  <https://orcid.org/0000-0003-1439-3610>
 David M. Long  <https://orcid.org/0000-0003-3137-0277>
 D. Shaun Bloomfield  <https://orcid.org/0000-0002-4183-9895>
 Ryun-Young Kwon  <https://orcid.org/0000-0002-2106-9168>
 Astrid M. Veronig  <https://orcid.org/0000-0003-2073-002X>
 Angelos Vourlidas  <https://orcid.org/0000-0002-8164-5948>
 Bojan Vršnak  <https://orcid.org/0000-0002-0248-4681>

References

Afanasyev, A. N., & Uralov, A. M. 2011, *SoPh*, **273**, 479
 Attrill, G. D. R., Harra, L. K., van Driel-Gesztelyi, L., & Démoulin, P. 2007, *ApJL*, **656**, L101
 Attrill, G. D. R., Long, D. M., Green, L. M., Harra, L. K., & van Driel-Gesztelyi, L. 2014, *ApJ*, **796**, 55
 Ballai, I. 2007, *SoPh*, **246**, 177
 Byrne, J. P., Long, D. M., Gallagher, P. T., et al. 2013, *A&A*, **557**, A96
 Chen, P. F., Wu, S. T., Shibata, K., & Fang, C. 2002, *ApJL*, **572**, L99
 Chen, P. F., & Wu, Y. 2011, *ApJL*, **732**, L20
 Cheung, M. C. M., Boerner, P., Schrijver, C. J., et al. 2015, *ApJ*, **807**, 143
 Cohen, O., Attrill, G. D. R., Manchester, W. B., & Wills-Davey, M. J. 2009, *ApJ*, **705**, 587
 Delaboudinière, J. P., Artzner, G. E., Brunaud, J., et al. 1995, *SoPh*, **162**, 291
 Delannée, C., Török, T., Aulanier, G., & Hochedez, J.-F. 2008, *Solar Phys*, **247**, 123

Dere, K. P., Brueckner, G. E., Howard, R. A., et al. 1997, *SoPh*, **175**, 601
 Dissauer, K., Temmer, M., Veronig, A. M., Vanninathan, K., & Magdalenic, J. 2016, *ApJ*, **830**, 92
 Domingo, V., Fleck, B., & Poland, A. I. 1995, *SoPh*, **162**, 1
 Downs, C., Linker, J. A., Mikić, Z., et al. 2013, *Sci*, **340**, 1196
 Downs, C., Roussev, I. I., van der Holst, B., et al. 2011, *ApJ*, **728**, 2
 Downs, C., Roussev, I. I., van der Holst, B., Lugaz, N., & Sokolov, I. V. 2012, *ApJ*, **750**, 134
 Downs, C., Török, T., Titov, V. S., et al. 2021, *ApJ*, in press
 Freeland, S. L., & Handy, B. N. 1998, *SoPh*, **182**, 497
 Gopalswamy, N., Yashiro, S., Temmer, M., et al. 2009, *ApJL*, **691**, L123
 Hannah, I. G., & Kontar, E. P. 2013, *A&A*, **553**, A10
 Harra, L. K., Sterling, A. C., Gömöry, P., & Veronig, A. 2011, *ApJL*, **737**, L4
 Hoilijoki, S., Pomoell, J., Vainio, R., Palmroth, M., & Koskinen, H. E. J. 2013, *SoPh*, **286**, 493
 Kaiser, M. L., Kucera, T. A., Davila, J. M., et al. 2008, *SSRv*, **136**, 5
 Kienreich, I. W., Muhr, N., Veronig, A. M., et al. 2013, *SoPh*, **286**, 201
 Kienreich, I. W., Temmer, M., & Veronig, A. M. 2009, *ApJL*, **703**, L118
 Kienreich, I. W., Veronig, A. M., Muhr, N., et al. 2011, *ApJL*, **727**, L43
 Klassen, A., Aurass, H., Mann, G., & Thompson, B. J. 2000, *A&AS*, **141**, 357
 Kwon, R.-Y., Kramar, M., Wang, T., et al. 2013, *ApJ*, **776**, 55
 Kwon, R.-Y., & Vourlidas, A. 2017, *ApJ*, **836**, 246
 Kwon, R.-Y., Zhang, J., & Olmedo, O. 2014, *ApJ*, **794**, 148
 Landi, E., Young, P. R., Dere, K. P., Del Zanna, G., & Mason, H. E. 2013, *ApJ*, **763**, 86
 Lario, D., Raouafi, N. E., Kwon, R.-Y., et al. 2014, *ApJ*, **797**, 8
 Lemen, J. R., Title, A. M., Akin, D. J., et al. 2012, *SoPh*, **275**, 17
 Lionello, R., Linker, J. A., & Mikić, Z. 2009, *ApJ*, **690**, 902
 Liu, W., Jin, M., Downs, C., et al. 2018, *ApJL*, **864**, L24
 Liu, W., Nitta, N. V., Schrijver, C. J., Title, A. M., & Tarbell, T. D. 2010, *ApJL*, **723**, L53
 Liu, W., & Ofman, L. 2014, *SoPh*, **289**, 3233
 Long, D. M., Bloomfield, D. S., Chen, P. F., et al. 2017b, *SoPh*, **292**, 7
 Long, D. M., Bloomfield, D. S., Gallagher, P. T., & Pérez-Suárez, D. 2014, *SoPh*, **289**, 3279
 Long, D. M., Gallagher, P. T., McAteer, R. T. J., & Bloomfield, D. S. 2008, *ApJL*, **680**, L81
 Long, D. M., Jenkins, J., & Valori, G. 2019, *ApJ*, **882**, 90
 Long, D. M., Murphy, P., Graham, G., Carley, E. P., & Pérez-Suárez, D. 2017a, *SoPh*, **292**, 185
 Long, D. M., Williams, D. R., Régnier, S., & Harra, L. K. 2013, *SoPh*, **288**, 567
 Lulić, S., Vršnak, B., Žic, T., et al. 2013, *SoPh*, **286**, 509
 Ma, S., Raymond, J. C., Golub, L., et al. 2011, *ApJ*, **738**, 160
 Ma, S., Wills-Davey, M. J., Lin, J., et al. 2009, *ApJ*, **707**, 503
 Mann, G. 1995, *JPIPh*, **53**, 109
 Mann, G., Klassen, A., Estel, C., & Thompson, B. J. 1999, in *ESA Special Publication*, Vol. 446, 8th SOHO Workshop: Plasma Dynamics and Diagnostics in the Solar Transition Region and Corona, ed. J.-C. Vial & B. Kaldeich-Schumann (Noordwijk: ESA), 477
 Miklenic, C., Veronig, A. M., Temmer, M., Möstl, C., & Biernat, H. K. 2011, *SoPh*, **273**, 125
 Moreton, G. E. 1960, *AJ*, **65**, 494
 Moreton, G. E., & Ramsey, H. E. 1960, *PASP*, **72**, 357
 Moses, D., Clette, F., Delaboudinière, J. P., et al. 1997, *SoPh*, **175**, 571
 Möstl, C., Rollett, T., Frahm, R. A., et al. 2015, *NatCo*, **6**, 7135
 Muhr, N., Veronig, A. M., Kienreich, I. W., et al. 2014, *SoPh*, **289**, 4563
 Muhr, N., Veronig, A. M., Kienreich, I. W., Temmer, M., & Vršnak, B. 2011, *ApJ*, **739**, 89
 Muhr, N., Vršnak, B., Temmer, M., Veronig, A. M., & Magdalenic, J. 2010, *ApJ*, **708**, 1639
 Nitta, N. V., Schrijver, C. J., Title, A. M., & Liu, W. 2013, *ApJ*, **776**, 58
 Olmedo, O., Vourlidas, A., Zhang, J., & Cheng, X. 2012, *ApJ*, **756**, 143
 Patsourakos, S., & Vourlidas, A. 2009, *ApJL*, **700**, L182
 Patsourakos, S., & Vourlidas, A. 2012, *SoPh*, **281**, 187
 Patsourakos, S., Vourlidas, A., & Kliem, B. 2010a, *A&A*, **522**, A100
 Patsourakos, S., Vourlidas, A., & Stenborg, G. 2010b, *ApJL*, **724**, L188
 Pesnell, W. D., Thompson, B. J., & Chamberlin, P. C. 2012, *SoPh*, **275**, 3
 Piantischitsch, I., Vršnak, B., Hanslmeier, A., et al. 2017, *ApJ*, **850**, 88
 Piantischitsch, I., Vršnak, B., Hanslmeier, A., et al. 2018a, *ApJ*, **857**, 130
 Piantischitsch, I., Vršnak, B., Hanslmeier, A., et al. 2018b, *ApJ*, **860**, 24
 Podladchikova, O., & Berghmans, D. 2005, *SoPh*, **228**, 265
 Podladchikova, T., Veronig, A. M., Dissauer, K., Temmer, M., & Podladchikova, O. 2019, *ApJ*, **877**, 68
 Santandrea, S., Gantois, K., Strauch, K., et al. 2013, *SoPh*, **286**, 5

- Schmidt, J. M., & Ofman, L. 2010, [ApJ](#), **713**, 1008
- Schrijver, C. J., Aulanier, G., Title, A. M., Pariat, E., & Delannée, C. 2011, [ApJ](#), **738**, 167
- Schrijver, C. J., & De Rosa, M. L. 2003, [SoPh](#), **212**, 165
- Seaton, D. B., Berghmans, D., Nicula, B., et al. 2013, [SoPh](#), **286**, 43
- Seaton, D. B., & Darnel, J. M. 2018, [ApJL](#), **852**, L9
- Shibata, K., & Magara, T. 2011, [LRSP](#), **8**, 6
- Temmer, M., Veronig, A. M., Gopalswamy, N., & Yashiro, S. 2011, [SoPh](#), **273**, 421
- Thompson, B. J., Plunkett, S. P., Gurman, J. B., et al. 1998, [GeoRL](#), **25**, 2465
- Titov, V. S., Török, T., Mikic, Z., & Linker, J. A. 2014, [ApJ](#), **790**, 163
- Török, T., Downs, C., Linker, J. A., et al. 2018, [ApJ](#), **856**, 75
- Uchida, Y. 1968, [SoPh](#), **4**, 30
- Vanninathan, K., Veronig, A. M., Dissauer, K., et al. 2015, [ApJ](#), **812**, 173
- Veronig, A. M., Gömöry, P., Kienreich, I. W., et al. 2011, [ApJL](#), **743**, L10
- Veronig, A. M., Muhr, N., Kienreich, I. W., Temmer, M., & Vršnak, B. 2010, [ApJL](#), **716**, L57
- Veronig, A. M., Podladchikova, T., Dissauer, K., et al. 2018, [ApJ](#), **868**, 107
- Veronig, A. M., Temmer, M., & Vršnak, B. 2008, [ApJL](#), **681**, L113
- Vršnak, B., & Cliver, E. W. 2008, [SoPh](#), **253**, 215
- Vršnak, B., Warmuth, A., Brajša, R., & Hanslmeier, A. 2002, [A&A](#), **394**, 299
- Vršnak, B., Žic, T., Lulić, S., Temmer, M., & Veronig, A. M. 2016, [SoPh](#), **291**, 89
- Wang, H., Shen, C., & Lin, J. 2009, [ApJ](#), **700**, 1716
- Wang, Y.-M. 2000, [ApJ](#), **543**, L89
- Warmuth, A. 2010, [AdSpR](#), **45**, 527
- Warmuth, A. 2015, [LRSP](#), **12**, 3
- Warmuth, A., & Mann, G. 2005, [A&A](#), **435**, 1123
- Warmuth, A., & Mann, G. 2011, [A&A](#), **532**, A151
- Warmuth, A., Shibasaki, K., Iwai, K., & Mann, G. 2016, [A&A](#), **593**, A102
- Warmuth, A., Vršnak, B., Aurass, H., & Hanslmeier, A. 2001, [ApJL](#), **560**, L105
- Warmuth, A., Vršnak, B., Magdalenic, J., Hanslmeier, A., & Otruba, W. 2004a, [A&A](#), **418**, 1117
- Warmuth, A., Vršnak, B., Magdalenic, J., Hanslmeier, A., & Otruba, W. 2004b, [A&A](#), **418**, 1101
- West, M. J., Zhukov, A. N., Dolla, L., & Rodriguez, L. 2011, [ApJ](#), **730**, 122
- Wills-Davey, M. J., DeForest, C. E., & Stenflo, J. O. 2007, [ApJ](#), **664**, 556
- Wuelser, J.-P., Lemen, J. R., Tarbell, T. D., et al. 2004, [Proc. SPIE](#), **5171**, 111
- Zhukov, A. N., & Auchère, F. 2004, [A&A](#), **427**, 705